N-Substituted Valiolamine Derivatives as Potent Inhibitors of Endoplasmic Reticulum α-Glucosidases I and II with Antiviral Activity

Journal:	*Journal of Medicinal Chemistry*
Manuscript ID	jm-2021-01377k.R2
Manuscript Type:	Article
Date Submitted by the Author:	04-Nov-2021
Complete List of Authors:	Karade, Sharanbasappa; Institute for Bioscience and Biotechnology Research, Hill, Michelle; University of Oxford, Department of Biochemistry Kiappes, John; University College London, Department of Chemistry Manne, Rajkumar; SAI Life Sciences Ltd Aakula, Balakishan; SAI Life Sciences Ltd Zitzmann, Nicole; University of Oxford, Department of Biochemistry Warfield, Kelly; Emergent BioSolutions Inc Treston, Anthony; Emergent BioSolutions Inc Mariuzza, Roy; University of Maryland Biotechnology Institute, Center for Advanced Research in Biotechnology

N-Substituted Valiolamine Derivatives as Potent Inhibitors of Endoplasmic Reticulum α-Glucosidases I and II with Antiviral Activity

Sharanbasappa S. Karade[1,2], Michelle L. Hill[3], J. L. Kiappes[4], Rajkumar Manne[5], Balakishan Aakula[5], Nicole Zitzmann[3], Kelly L. Warfield[6], Anthony M. Treston[6], and Roy A. Mariuzza[1,2]*

[1]University of Maryland Institute for Bioscience and Biotechnology Research, Rockville, MD 20850, USA

[2]Department of Cell Biology and Molecular Genetics, University of Maryland, College Park, MD 20742, USA

[3]Oxford Glycobiology Institute, Department of Biochemistry, University of Oxford, Oxford OX1 3QU, UK

[4]Department of Chemistry, University College, London WC1H 0AJ, UK

[5]Sai Life Sciences Ltd., 500032 Telangana, India

[6]Emergent BioSolutions, Gaithersburg, MD 20879, USA

ABSTRACT

Most enveloped viruses rely on host cell endoplasmic reticulum (ER) quality control (QC) machinery for proper folding of glycoproteins. The key ER α-glucosidases (α-Glu) I and II of the ERQC machinery are attractive targets for developing broad-spectrum antivirals. Iminosugars based on deoxynojirimycin have been extensively studied as ER α-glucosidase inhibitors, however other glycomimetic compounds are less established. Accordingly, we synthesized a series of *N*-substituted derivatives of valiolamine, the iminosugar scaffold of type 2 diabetes drug voglibose. To understand the basis for the up to 100,000-fold improved inhibitory potency, we determined high-resolution crystal structures of mouse ER α-GluII in complex with valiolamine and 10 derivatives. The structures revealed extensive interaction with all four α-GluII subsites. We further showed that *N*-substituted valiolamines were active against dengue virus and SARS-CoV-2 *in vitro*. This study introduces valiolamine-based inhibitors of the ERQC machinery as candidates for developing potential broad-spectrum therapeutics against existing and emerging viruses.

INTRODUCTION

Direct-acting antiviral agents (DAAs) combat viral infections by targeting viral proteins. Although DAAs such as RNA polymerase inhibitors for the treatment of hepatitis C virus (HCV) infections have been very successful in the clinic, DAAs suffer from several inherent limitations[1]. Because viral proteins do not typically share structural similarity among different virus families, a DAA targeting a specific viral protein is unlikely to impart the same inhibitory effect against different viruses (narrow-spectrum antivirals). In addition, DAAs often have low genetic barriers to drug resistance due to selective pressure during virus replication. For example, the ability of HCV to evolve rapidly and the existence of natural polymorphisms associated with resistance to DAAs endanger the future success of currently successful anti-HCV therapies[2,3].

In contrast to DAAs, host-targeting antivirals (HTAVs) are directed against host proteins required for virus replication[1,4,5]. Because a specific host protein might play critical roles in the replication of several types of viruses, HTAVs could potentially treat a wide spectrum of viral infections (broad-spectrum antivirals). For example, heat shock protein 90 (Hsp90) is a host chaperone required for proper folding and assembly of endogenous proteins. Because this chaperone is also crucial for the maturation of many viral proteins, Hsp90 inhibitors possess broad-spectrum antiviral activities[6]. Targeting of virus–host interactions is also an attractive strategy to avoid antiviral drug resistance arising from escape mutations in the viral genome.

Most enveloped viruses rely heavily on the host cell endoplasmic reticulum (ER) glycoprotein quality control (QC) machinery for correct folding of their surface glycoproteins[7]. Inhibition of the ERQC machinery causes viral glycoproteins to misfold and prevents the formation of mature, infectious virions[7-9]. ER α-glucosidases I and II (α-GluI and α-GluII) are key components of the ERQC machinery[10,11], making them attractive targets for developing broad-

spectrum antivirals[1,9]. These glycoside hydrolases catalyze sequential removal of terminal glucoses from the $Glc_3Man_9GlcNAc_2$ *N*-linked glycan attached to nascent glycoproteins. The interaction of monoglucosylated ($Glc_1Man_9GlcNAc_2$) glycoproteins with the ER chaperones calnexin and calreticulin protects folding intermediates from aggregation or premature export. Removal of the final glucose by α-GluII leaves glycoproteins with a $Man_9GlcNAc_2$ glycan and prevents them from interacting with the ER chaperones. If correctly folded, the trimmed glycoproteins are then free to proceed to the Golgi apparatus and secretion[10,11]. If not correctly folded yet, the glycoproteins will be re-glucosylated by UDP-glucose glucosyltransferase, making them substrates again for calnexin/calreticulin. If permanently misfolded, removal of a mannose residue will mark the glycoprotein for degradation by the ER associated degradation pathway.

Glucose-mimicking compounds that competitively inhibit ER α-GluI and α-GluII have demonstrated *in vitro* and, in some cases, *in vivo* antiviral efficacy against representative members of multiple viral families, including *Flavi-*, *Rhabdo-*, *Herpes-*, *Hepadna-*, *Toga-*, *Retro-*, *Arena-*, *Orthomyxo-*, and *Paramyxoviridae* [9,12]. By far the best studied inhibitors of α-GluI and α-GluII are iminosugars[13,14], in which a nitrogen atom has replaced oxygen in the sugar ring. Several iminosugar derivatives, notably *N*-9'-methoxynonyl 1-deoxynojirimycin (UV-4 or M*O*N-DNJ), have antiviral activity *in vivo* against dengue virus[15,16], influenza A (H1N1)[17], and influenza B[18] with no reported toxicity in mouse models. Collectively, these results support the development of inhibitors of host ER α-glucosidases as potential broad-spectrum therapeutics against existing and newly emerging viruses, such as severe acute respiratory syndrome coronavirus 2 (SARS-CoV-2)[19,20].

The search for compounds to treat type 2 diabetes by preventing saccharide hydrolysis has led to three clinically approved inhibitors of intestinal (as opposed to ER) α-glucosidases: miglitol,

acarbose, and voglibose[21]. These glycomimetics employ different amino sugar scaffolds: the iminosugar 1-deoxynojirimycin (DNJ) for miglitol, valienamine ((1S,2S,3R,6S)-6-amino-4-(hydroxymethyl)cyclohex-4-ene-1,2,3-triol) for acarbose, and valiolamine ((1S,2*S*,3*R*,4*S*,5*S*)-5-amino-1-(hydroxymethyl)cyclohexane-1,2,3,4-tetraol) for voglibose[22,23]. Whereas iminosugars based on DNJ have been studied extensively as ER α-glucosidase inhibitors and potential antiviral therapeutics[12-18], as noted above, valienamines and valiolamines, which contain an exocyclic amine group, have not, with the exception of several valienamine derivatives that showed limited α-GluII inhibitory activity[24]. Accordingly, we synthesized a series of *N*-substituted valiolamine derivatives, measured their ability to inhibit ER α-GluI and α-GluII, and tested them for activity against dengue virus and SARS-CoV-2 *in vitro*. We determined high-resolution crystal structures of α-GluII in complex with valiolamine and 10 valiolamine derivatives. The structures explain the basis for the 10,000–100,000-fold greater inhibitory potency of some of these derivatives against ER α-glucosidase II compared to valiolamine itself. In addition, the α-GluII–inhibitor complexes provide a foundation for structure-guided discovery of drug candidates against diabetes, known viruses, and those yet to be discovered.

RESULTS AND DISCUSSION

Structure Determination of α-GluII–Inhibitor Complexes. Eukaryotic α-GluII is a soluble heterodimeric ER protein composed of a catalytic α subunit and an accessory β subunit. The α subunit belongs to the GH31 family of glycoside hydrolases. The structure of mouse α-GluII was determined previously[25]. Importantly, all active site residues are strictly conserved in mouse and human α-GluII, making mouse α-GluII a suitable surrogate for the human enzyme in studying interactions with inhibitors. The original crystallization of mouse α-GluII required trypsin

digestion of the full-length enzyme, resulting in elimination of most of the non-catalytic β subunit. We were likewise unable to crystallize full-length α-GluII, but did obtain crystals after trypsinization (α-GluII$_{Tryp}$). However, our α-GluII$_{Tryp}$ crystals, which grew under conditions different from those described previously[25], belonged to a primitive orthorhombic space group with extra screw at the *z*-axis ($P2_12_12_1$ versus $P2_12_12$) and diffracted to only ~3.5 Å resolution, which is insufficient to delineate α-GluII–inhibitor interactions at the atomic level. We nevertheless solved the α-GluII$_{Tryp}$ structure in this new space group by molecular replacement and observed a glycan moiety attached to Asn97 of the α subunit, a reported *N*-glycosylation site[25]. This glycan contacts a symmetry-related α-GluII$_{Tryp}$ molecule in the crystal. Reasoning that these contacts might be deleterious to lattice formation, we eliminated the *N*-glycosylation site at Asn97 by mutating this residue to aspartate. This modification, combined with glutaraldehyde cross-linking (Experimental section), yielded crystals belonging to a different space group ($P3_2$) that enabled us to determine the mutant apo α-GluII$_{Tryp}$ structure to 2.29 Å resolution (Fig. 1*A*). Superposition onto the wild-type apo α-GluII$_{Tryp}$ structure[25] gave a root-mean-square difference (r.m.s.d.) in Cα-carbon positions of 0.3 Å, indicating close similarity.

To prepare α-GluII–inhibitor complexes, crystals of apo α-GluII$_{Tryp}$ were soaked in inhibitor solutions. We determined structures of 11 α-GluII$_{Tryp}$–inhibitor complexes to resolutions ranging from 2.07 Å to 2.55 Å (Supplementary Table 1). The structures showed unambiguous electron density for all 11 inhibitors in the α-GluII active site (Fig. 2). We first describe key features of the α-GluII active site of relevance to inhibitor design, and then present structures of the α-GluII–inhibitor complexes.

Structure of Apo ER α-GluII. The α-GluII$_{Tryp}$ structure comprises an intact catalytic α subunit and a portion of the accessory β subunit containing two tandem low-density lipoprotein receptor class A (LDLRa) domains that remain associated with the α subunit after trypsinization (Fig. 1A). The α subunit active site is further divided into four subsites, designated –1, +1, +2, and +3 (Fig. 1B). Residues forming the –1 and +1 subsites are highly conserved across α-glucosidases of the GH31 family, with Asp564 acting as the catalytic nucleophile and Asp640 as the acid/base catalyst (residue numbers correspond to mouse α-GluII). The less conserved +2 and +3 subsites are decorated by aromatic residues, notably Phe307, Trp523, Trp525, and Phe571. Whereas most residues lining the –1 and +1 subsites of α-GluII are identical to those in intestinal glucosidases, such as sucrase-isomaltase (SI) and maltase-glucoamylase (MGAM), the +2 subsite of α-GluII is smaller than in SI or MGAM due to a two-residue insertion (Phe307 and Gln308), which is absent in other GH31 family members (Fig. 1B). This insertion is located in a loop (residues 305–317), termed the exclusion loop[25], that flanks the catalytic site (Fig. 1A).

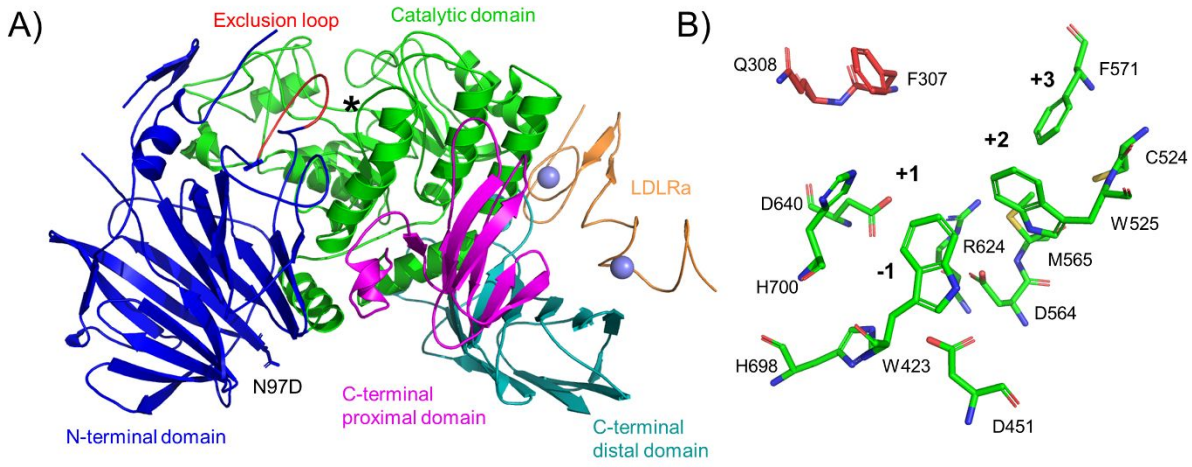

Figure 1. Crystal structure of apo mouse α-glucosidase II (PDB accession code 7L9E). (A) Overall view of α-GluII (ribbon diagram). The structure comprises a catalytic α subunit and an accessory

β subunit. The GH31 catalytic domain of the α subunit is green. The exclusion loop in the catalytic domain that contains the Phe307, Gln308 insertion is red. The N-terminal domain of the α subunit is blue; its proximal and distal C-terminal domains are magenta and teal, respectively. The trypsinized β subunit contains two tandem LDLRa domains (orange). Two calcium ions in the LDLRa domains are drawn as light blue spheres. The location of the active site in the GH31 catalytic domain is indicated by an asterisk. The Asn97Asp mutation (N97D) in the α subunit N-terminal domain is distant (~40 Å) from the active site. (B) Close-up view of the α-GluII active site. Subsites –1, +1, +2, and +3 are labelled. Asp564 acts as the catalytic nucleophile and Asp640 as the acid/base catalyst[25]. Residues Phe307 and Gln308 in the exclusion loop are shown in red.

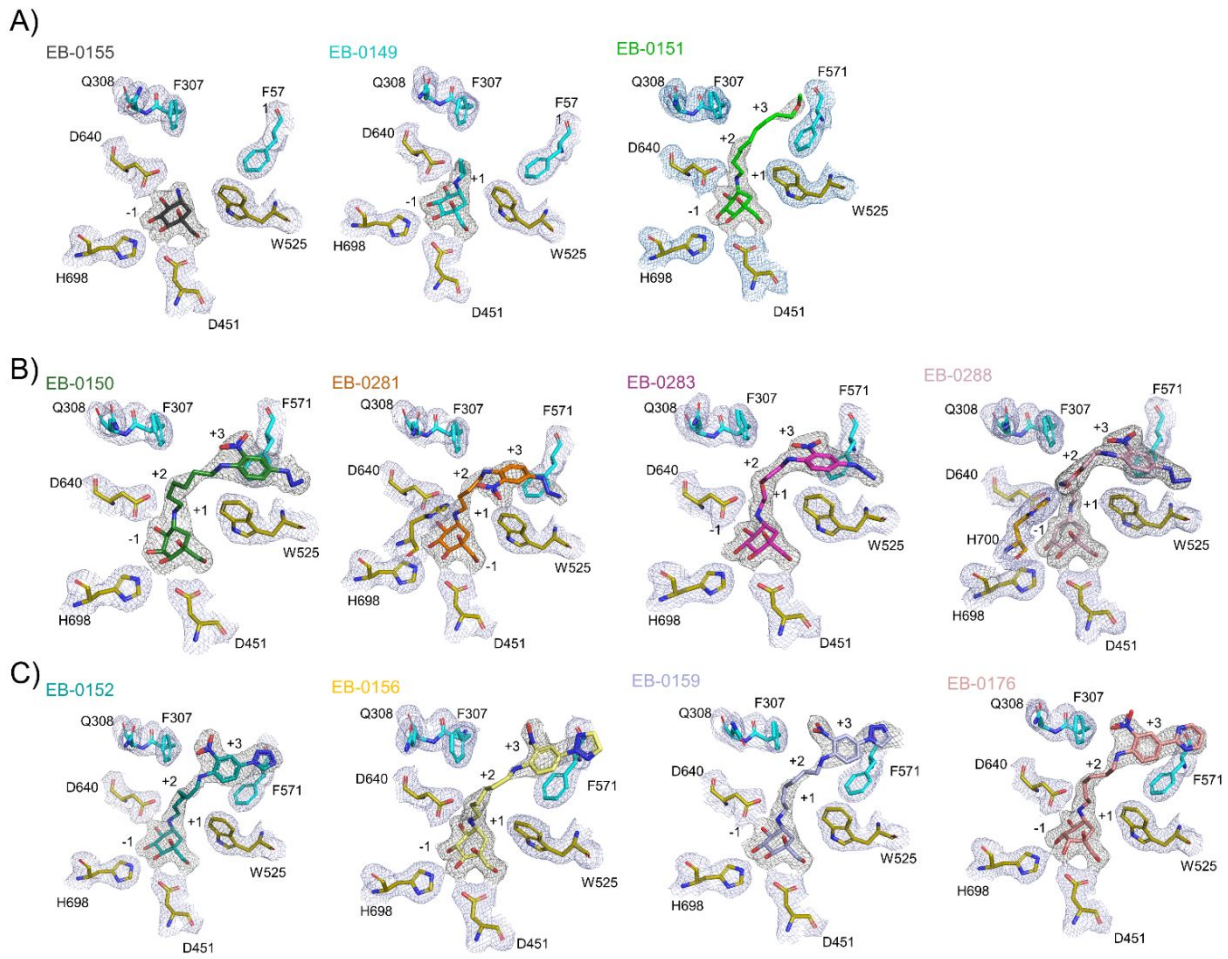

Figure 2. Electron densities for valiolamine and *N*-substituted valiolamine derivatives bound to the active site of ER α-GluII. (A) Complexes with EB-0155, EB-0149, and EB-0151. (B) Complexes with EB-0150, EB-0281, EB-0283, and EB-0288. (C) Complexes with EB-0152, EB-0156, EB-0159, and EB-0176. For each complex, density from the final $2F_o - F_c$ map is contoured at 1σ. Subsites –1, +1, +2, and +3 are labelled where the respective inhibitors approach or interact with the subsites.

Design and Synthesis of Valiolamine-based Inhibitors. Based on the structure of the α-GluII active site (Fig. 1B), we synthesized a set of *N*-substituted valiolamine derivatives (Experimental section) designed to potentially interact with all four subsites of this enzyme (Table 1). The

synthetic schemes for the majority of targets, for which similar approaches were used, are summarized in Schemes 1 and 2, and the independent scheme for EB-0288 is shown in Scheme 3. We reasoned that targeting the –1 and +1 subsites of α-GluII, which are conserved in other α-glucosidases, as well as the more variable +2 and +3 subsites, should lead to inhibitors with increased potency and selectivity for α-GluII. In particular, the cluster of aromatic residues lining the +2 and +3 subsites (Phe307, Trp523, Trp525, and Phe571) should constitute an attractive target for such inhibitors. Of note, exclusion loop residue Phe307 is unique to ER α-GluII enzymes and is missing from intestinal glucosidases.

As described above, glycomimetics iminosugars incorporating valiolamine and the closely-related valienamine are present in drugs approved for treating Type II diabetes and known to inhibit gastrointestinal GH31 glycoside hydrolases (21). In addition to valiolamine itself (EB-0155), 10 *N*-alkylated derivatives of valiolamine were synthesized and examined (Table 1). These derivatives differ by the length of the alkyl chain and by the absence (EB-0149, EB-0151) or presence (EB-0150, EB-0281, EB-0283, EB-0288, EB-0152, EB-0156, EB-0159, EB-0176) of an aminophenyl moiety attached to the alkyl chain. Among the eight aminophenyl-containing derivatives, four (EB-0150, EB-0281, EB-0283, EB-0288) have nitroxide and azide groups attached to the aminophenyl ring, but differ in the length and/or composition of the alkyl chain (Table 1). This aryl ring was chosen based on the reported NAP-DNJ (N-(N-4-azido-2-nitrophenyl)-6-aminohexyl-DNJ, also called UV-5), which is a high-potency inhibitor of mammalian ER α-GluII[25] and a recognized antiviral agent[26]. Incorporation of the nitroxide-azido-aryl ring into these valiolamine derivatives also allowed for possible cross-linking of these tool compounds to the enzyme in future studies. In addition to a nitroxide, the other four aminophenyl-containing derivatives have a tetrazole (EB-0152), triazole (EB-0156, EB-0159), or pyrimidine

(EB-0176) group attached to the aminophenyl ring, which is linked to valiolamine via a 1,6-hexamethylene alkyl chain.

Table 1. Inhibition (IC_{50}) of α-GluI and α-GluII by Valiolamine and Valiolamine Derivatives

Compound	Molecular structure	α-GluI IC_{50} (μM)	α-GluII IC_{50} (μM)
EB-0155	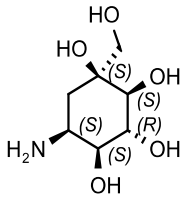	87.39	>100
EB-0149	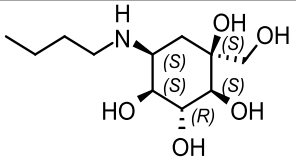	29.54	38.69
EB-0151	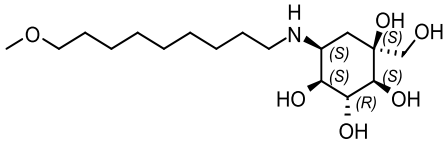	10.77	0.4902
EB-0150	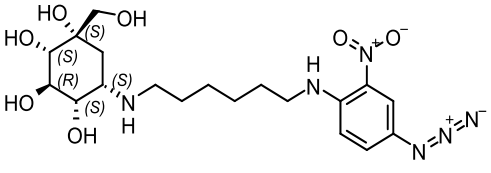	0.73	0.0337

EB-0281	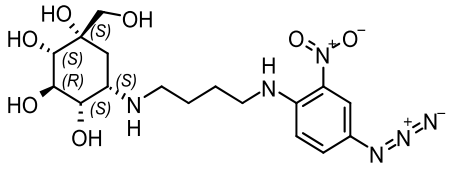	2.422	1.01
EB-0283	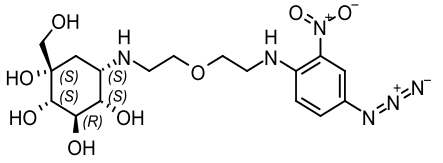	3.664	37.0
EB-0288	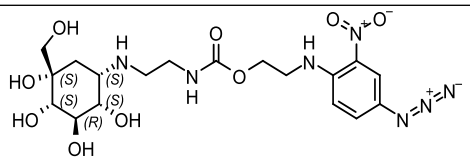	1.1284	N.D.
EB-0152	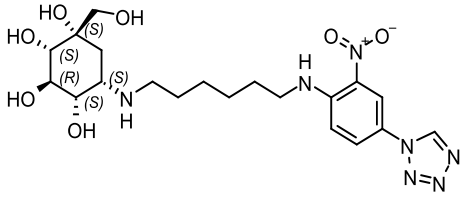	32.05	1.419
EB-0156	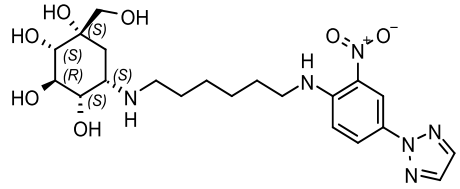	0.0479	<0.001
EB-0159	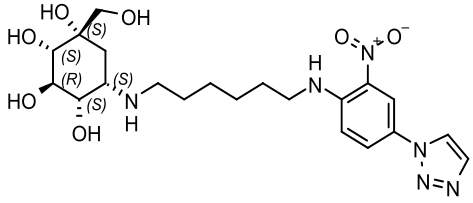	1.27	0.0155
EB-0176	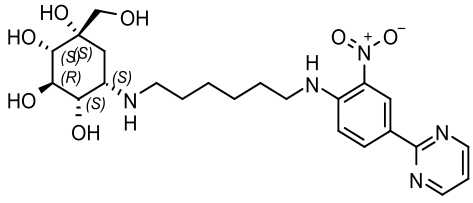	0.6439	0.0011

Structure of ER α-GluII–Inhibitor Complexes. In each α-GluII–inhibitor complex, the hydroxyl groups of the valiolamine moiety form conserved hydrogen bonds with –1 subsite residues Asp451, Arg624, Asp640, and His698 (Fig. 3). In addition to these conventional hydrogen bonds (X–H···A, in which X and A are O or N atoms), the C-5' hydroxy of the valiolamine moiety makes an unconventional hydrogen bond (X–H···π)[27] with the π-electron cloud of Trp423 serving as the acceptor. These direct hydrogen bonds are reinforced by several conserved water-mediated hydrogen bonds involving –1 subsite residues.

Whereas the short alkyl chain of EB-0149 (4 atoms) fills only the +1 subsite, the long alkyl chain of EB-0151 (11 atoms) spans the +1, +2, and +3 subsites, making extensive hydrophobic contacts with aromatic residues Phe307, Phe571, Phe673, Phe674, and Trp525 (Fig. 3*A*). In contrast to valiolamine alone (EB-0155), which buries only 65 Å^2 of surface area upon complex formation, EB-0149 and EB-0151 bury 113 Å^2 and 216 Å^2, respectively, representing substantial increases in buried area. A dramatic improvement in inhibitory potency as a result of occupying progressively more subsites of α-GluII is evident by comparing IC_{50} values against the isolated enzyme: >100 μM for EB-0155 (valiolamine), 38.7 μM for EB-0149, and 0.49 μM for EB-0151 (Table 1). Of note, EB-0151 and the DNJ-based iminosugar derivative UV-4 share the same 11-atom alkyl chain and have similar inhibitory potencies (IC_{50} = 1.8 μM for UV-4)[28]. In the crystal structure of UV-4 bound to α-GluII[25], the alkyl chain of UV-4 clashes with Trp525 and induces disorder in the 523–528 loop, which is not the case for EB-0151 or any of the other *N*-substituted valiolamines in this study. Whereas modification of UV-4 at the endocyclic nitrogen of the DNJ

directs the alkyl chain towards Trp525, modification of valiolamine at the exocyclic nitrogen orients the alkyl chain away from this bulky residue.

The aminophenyl ring of all four derivatives with attached nitroxide and azide groups (EB-0150, EB-0281, EB-0283, EB-0288) fits in the +3 subsite (Fig. 3B). In each case, the aminophenyl ring is perpendicular to the indole ring of Trp525, with which it forms T-shaped π–π stacking interactions (Fig. 4A–D). Additionally, EB-0150 establishes an anion–π interaction with Phe571 via its nitroxide group (Fig. 4A). The length of the acyl chain linking the valiolamine and the aminophenyl moieties of the inhibitors determines whether there is a hydrogen bond between the aryl azide and the carbonyl oxygen of Cys524. This interaction is only possible if the linker exceeds 4 atoms, as in EB-0283 (5 atoms), EB-0150 (6 atoms), and EB-0288 (7 atoms) (Fig. 4A, C, D). The 4-atom linker of EB-0281 is too short to position its azide group within hydrogen bonding distance of Cys524 (Fig. 4B). Instead, the aminophenyl ring of EB-0281 makes sandwich π–π stacking interactions with the parallel phenyl ring of Phe571, thereby flipping the nitroxide group. The potential benefit of adding an aminophenyl moiety to the alkyl chain may be appreciated by comparing the IC_{50} of EB-0151 (0.49 μM), which has only an alkyl chain, with that of EB-0150 (34 nM) (Table 1). The longer the chain, the greater the amount of surface area buried in the complex with α-GluII: EB-0281 (4 atoms; 245 $Å^2$), EB-0283 (5 atoms; 254 $Å^2$), EB-0150 (6 atoms; 259 $Å^2$). However, improvement in inhibitory potency is dependent on the length and/or composition of the alkyl chain, since EB-0281 (IC_{50} = 1.0 μM) and EB-0283 (37 μM), which contain the same aminophenyl group as EB-0150, have comparable or worse IC_{50} values (1.0 μM and 37 μM, respectively) as EB-0151 (0.49 μM). Future studies will be required to delineate the impact of substitutions within the alkyl chain.

The best valiolamine-based α-GluII inhibitors, with up to 100,000-fold greater potency than valiolamine and up to 1,500-fold greater potency than UV-4[28], have a tetrazole (EB-0152), triazole (EB-0156, EB-0159), or pyrimidine (EB-0176) group, as well as a nitroxide, attached to an aminophenyl ring (Table 1). All four inhibitors span the –1, +1, +2, and +3 subsites (Fig. 1; Fig. 3C, D). The aminophenyl rings of EB-0152 and EB-0176 are perpendicular to the phenyl ring of Phe571, forming T-shaped π–π interactions (Fig. 5A, D), whereas the aminophenyl rings of EB-0156 and EB-0159 are parallel to the phenyl ring of Phe571, making sandwich π–π interactions (Fig. 5B, C). The aromatic triazole rings of EB-0156 and EB-0159 establish additional π–π interactions with Trp523 and Phe571. In the α-GluII–EB-0176 complex, the pyrimidine ring of EB-0176 forms a π–σ interaction with the β-carbon of Phe571, while one of the pyrimidine ring carbons makes a C–H···O hydrogen bond[29] with the carbonyl oxygen of Phe571 (Fig. 5D). The inhibitory potency of these derivatives against α-GluII spans a >1000-fold range: EB-0156 (IC_{50} < 1 nM) > EB-0176 (IC_{50} = 1.1 nM) > EB-0159 (16 nM) > EB-0152 (1.4 μM) (Table 1). The much lower potency of EB-0152 compared to EB-0156 or EB-0159 could be due to the absence of π–π interactions between the tetrazole ring of EB-0152 and Trp523 (Fig. 5A).

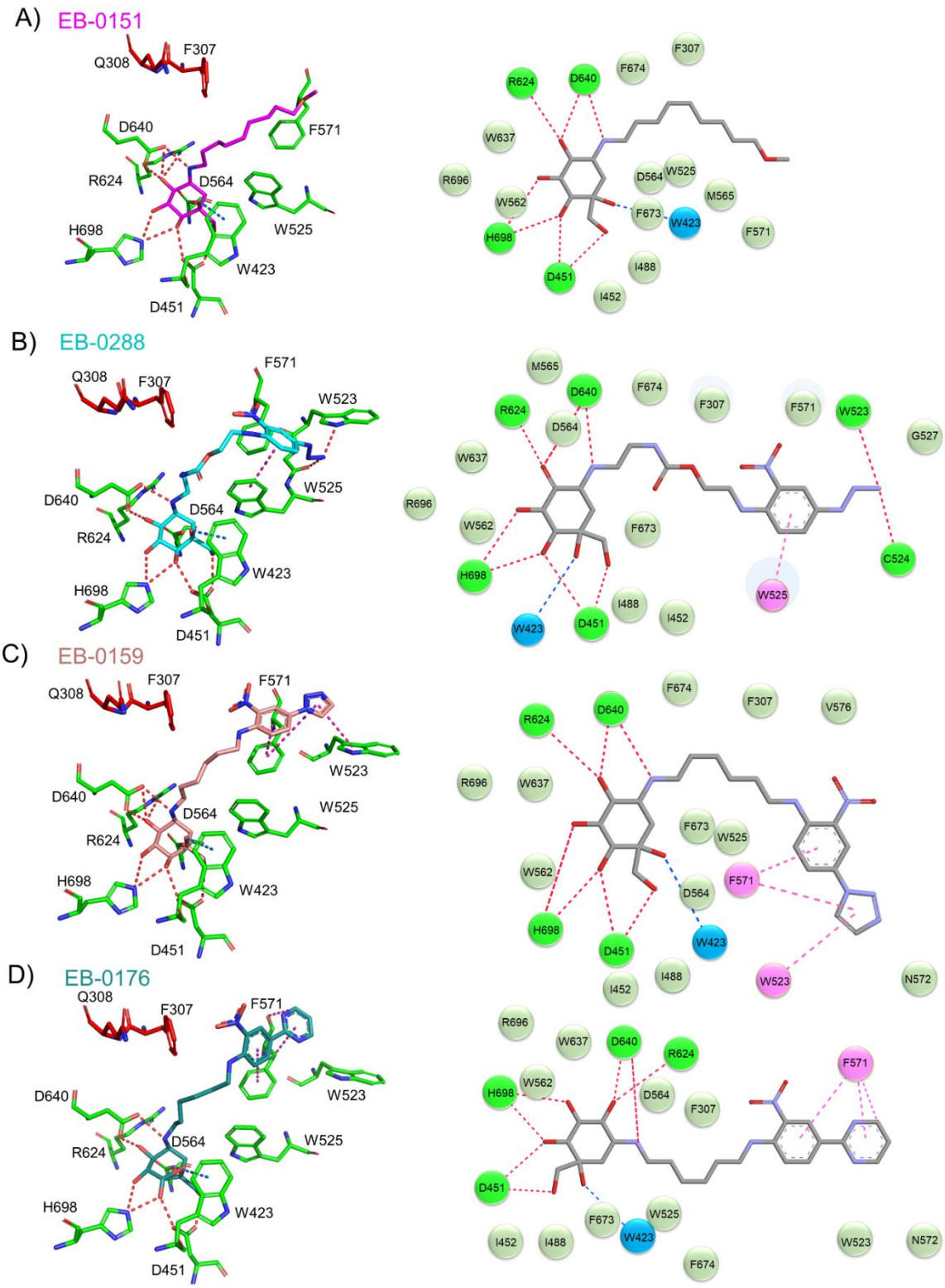

Figure 3. Structure of representative α-GluII–inhibitor complexes. (A) (left) Interaction of EB-0151 with α-GluII (PDB accession code 7K9N). The side chains of contacting residues of α-GluII

are shown in stick representation with carbon atoms in green (active site residues) or red (exclusion loop residues). The EB-0151 inhibitor is magenta. Conventional hydrogen bonds are depicted as red dotted lines. An unconventional hydrogen bond (O–H···π)[27] involving Trp423 is drawn as a blue dotted line. (right) Schematic representation of α-GluII–EB-0151 interactions. Active site residues forming conventional or O–H···π hydrogen bonds are shown as dark green or blue balls, respectively. Residues making van der Waals contacts with EB-0151 are light green balls. (B) (left) Interaction of EB-0288 (cyan) with α-GluII (7KBR). π–π interaction involving Trp525 is indicated by a magenta dotted line. (right) Schematic representation of α-GluII–EB-0288 interactions. Residue forming π–π interaction is a magenta ball. (C) (left) Interaction of EB-0159 (salmon) with α-GluII (7KAD). (right) Schematic representation of α-GluII–EB-0159 interactions. (D) (left) Interaction of EB-0176 (teal) with α-GluII (7KB6). (right) Schematic representation of α-GluII–EB-0176 interactions. The figure was generated by PyMOL (https://pymol.org/2/) and Discovery Studio (https://www.discngine.com/discovery-studio).

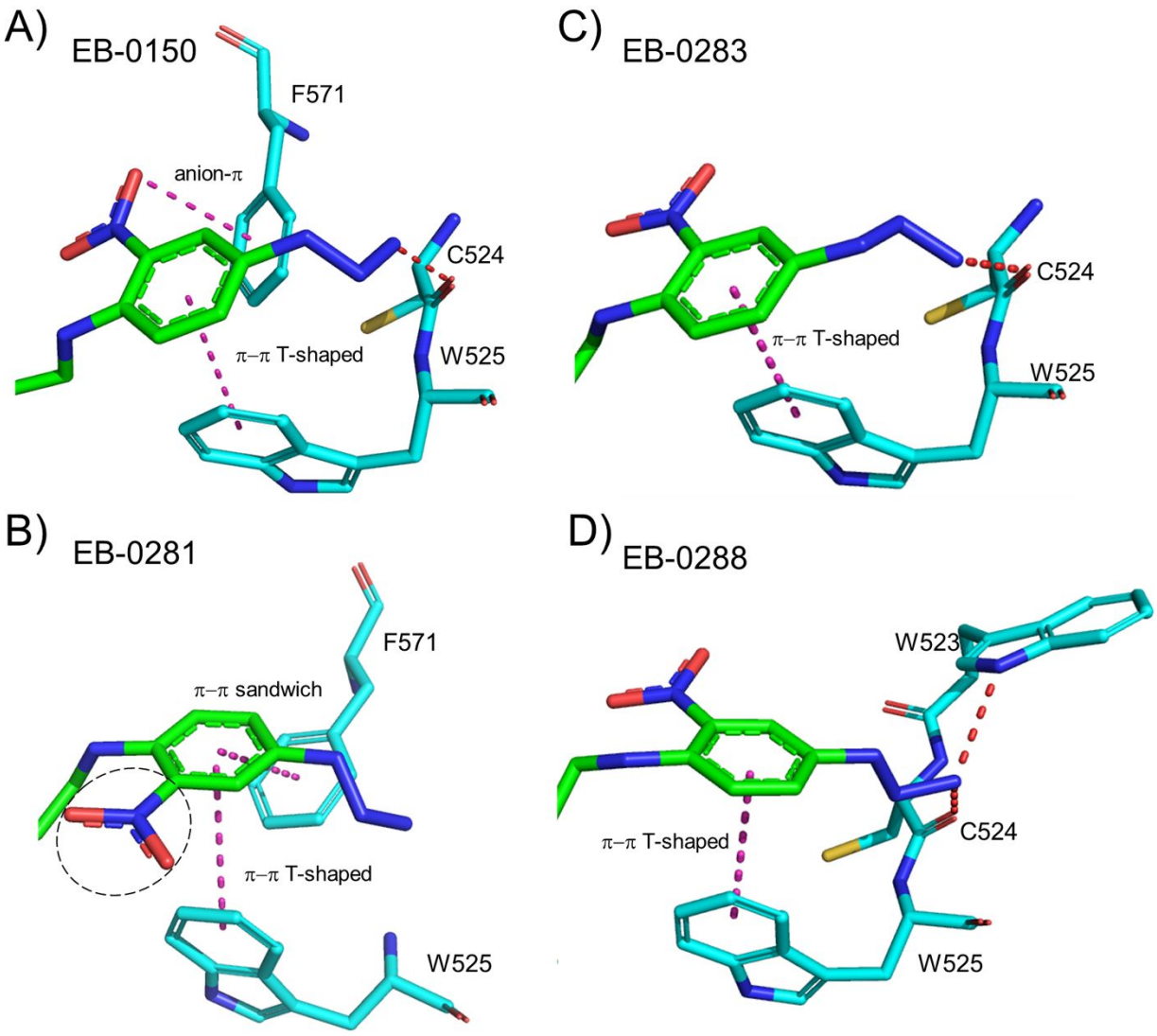

Figure 4. Interaction of (A) EB-0150 (PDB accession code 7KRY), (B) EB-0281 (7KB8), (C) EB-0283 (7KBJ), and (D) EB-0288 (7KBR) with +2 and +3 subsites of α-GluII. A T-shaped π–π interaction with Trp525 is conserved in all four complexes. EB-0150 forms an additional anion–π interaction with Phe571. The flipped nitroxide group of EB-0281 is circled. π interactions are indicated by magenta dotted lines and hydrogen bonds by red dotted lines.

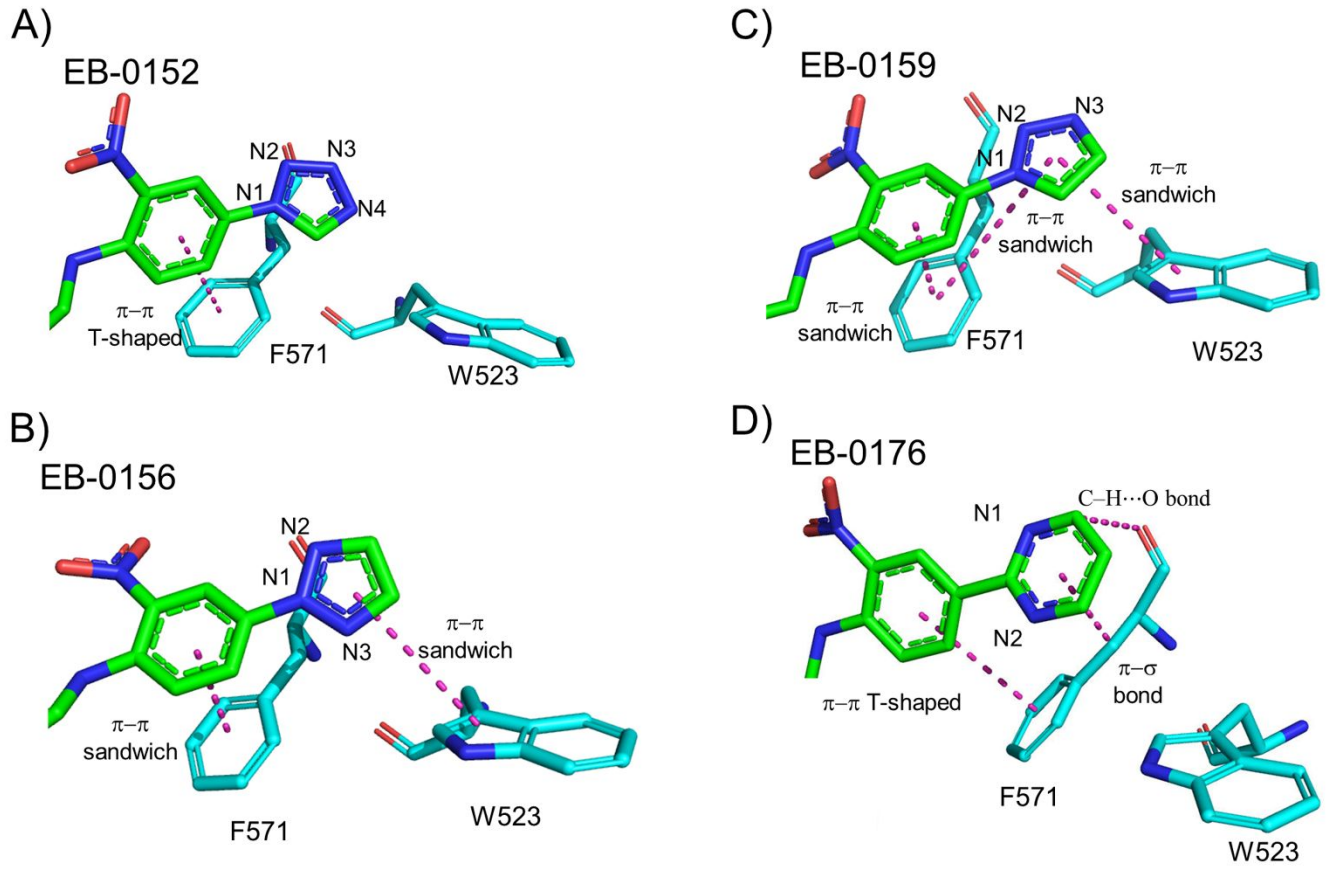

Figure 5. Interaction of (A) EB-0152 (PBD accession code 7K9O), (B) EB-0156 (7K9T), (C) EB-0159 (7KAD), and (D) EB-0176 (7KB6) with +2 and +3 subsites of α-GluII.

Dual Binding Modes of Valiolamine Derivatives. Superposition of the 11 α-GluII–inhibitor structures revealed that, whereas all the inhibitors align well at the –1 and +1 subsites, their alkyl chains follow two different paths at the +2 and +3 subsites (Fig. 6A). The alkyl chains of EB-0150, EB-0281, EB-0283, and EB-0288 diverge by ~45° from those of EB-0152, EB-0156, EB-0159, and EB-0176 starting at the junction between the +1 and +2 subsites. These dual binding modes are dictated by specific substituents on the aminophenyl ring attached to the alkyl chain. Thus, the azide group attached to the aminophenyl ring of EB-0150, EB-0281, EB-0283, and EB-0288 is sufficiently small to allow this ring to approach the indole ring of Trp525, with which it forms π–

π interactions (Fig. 4A–D). By contrast, the larger tetrazole, triazole, or pyrimidine group attached to the aminophenyl ring of EB-0152, EB-0156, EB-0159, and EB-0176 displaces the ring away from Trp525 and towards Phe571, resulting in the observed ~45° divergence in the direction of the alkyl chains (Fig. 6B).

Acarbose is a noncleavable α(1,4)-tetrasaccharide mimic that inhibits intestinal α-glucosidases and is used to treat type 2 diabetes. In the crystal structure of acarbose bound to human intestinal MGAM, a member of the same GH31 family of glycoside hydrolases as α-GluII, the first two rings of the nonreducing end of acarbose occupy the –1 and +1 subsites[30]. Superposition of acarbose onto EB-0283 and EB-0176 showed that all three inhibitors align well at the –1 and +1 subsites, but that acarbose diverges from EB-0288 and EB-0176 by ~140° and ~95°, respectively, at the +2 and +3 subsites (Fig. 6B). Acarbose cannot fit into the active site of α-GluII because of steric clashes with residues Phe307 and Gln308 in the exclusion loop of α-GluII, which are absent in MGAM and other GH31 family members.

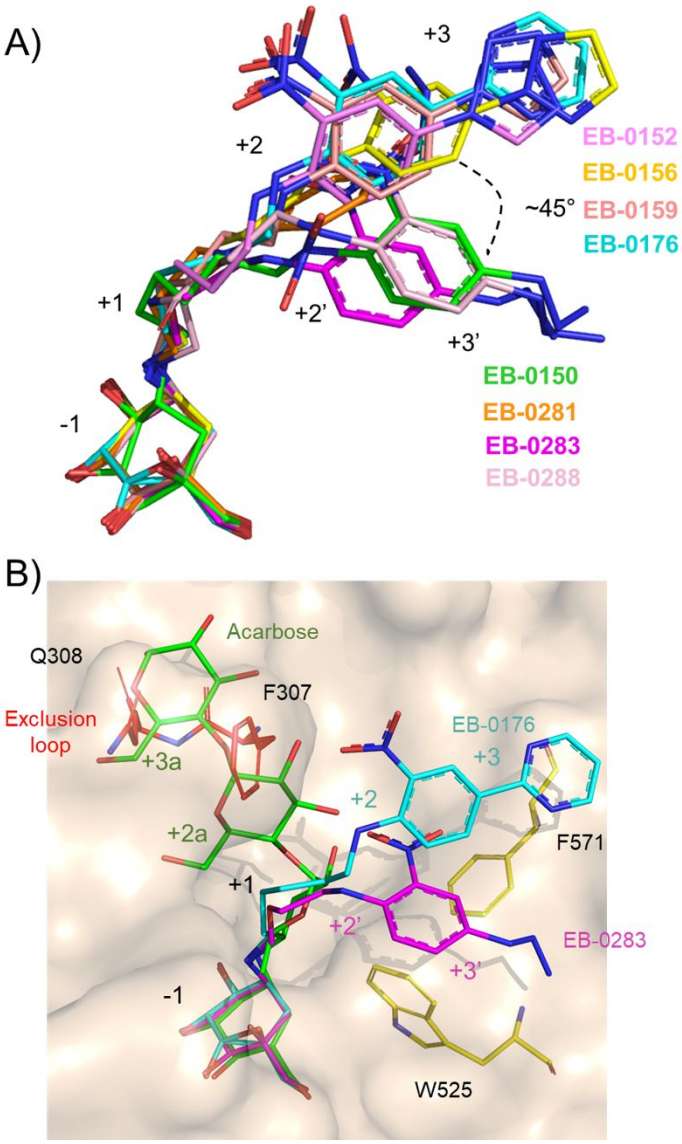

Figure 6. Dual binding modes of valiolamine-based inhibitors. (A) Superposition of eight inhibitors in their α-GluII-bound conformations. EB-0150 (PDB accession code 7KRY), EB-0281 (7KB8), EB-0283 (7KBJ), and EB-0288 (7KBR) diverge by ~45° from EB-0152 (7K9O), EB-0156 (7K9T), EB-0159 (7KAD), and EB-0176 (7KB6) at the +2 and +3 subsites. (B) Active site residues responsible for dual binding modes of EB-0283 and EB-0176 are yellow. Acarbose (green) in its MGAM-bound conformation (2QMJ)[30] was superposed onto EB-0283 and EB-0176.

Steric clashes with exclusion loop residues Phe307 and Gln308 (red) preclude acarbose binding to α-GluII.

Inhibition of ER α-Glucosidase I. A notable feature of the *N*-substituted valiolamines studied here is that they also inhibit ER mouse α-GluI, although generally not as well as α-GluII (Table 1). For example, EB-0176, one of our most potent α-GluII inhibitors (IC_{50} = 1.1 nM), inhibits α-GluI ~600-fold less well (IC_{50} = 0.6 μM). Two valiolamine derivatives (EB-0149 and EB-0281) have comparable IC_{50} values for α-GluI and α-GluII. As in the case of α-GluII, attachment of an alkyl chain and aminophenyl group to the valiolamine scaffold greatly improved inhibition of α-GluI (Table 1).

Cross-inhibition of α-GluI and α-GluII by the same set of valiolamines is surprising, given that these glycoside hydrolases belong to different families (GH63 and GH31, respectively). A comparison of the recently reported crystal structure of mouse ER α-GluI[31] with that of α-GluII revealed that, while the –1 and +1 subsites are relatively conserved, the +2 and +3 subsites diverge considerably. Nevertheless, the +2 and +3 subsites α-GluI, like those of α-GluII, are decorated by a cluster of aromatic residues, notably Phe440, Phe441, and Phe445. In the absence of crystal structures of α-GluI–inhibitor complexes, we used AutoDock4[32] to computationally dock EB-0150, EB-0176, and EB-0151 into the active site of α-GluI. As shown in Fig. 7, valiolamine occupies the –1 subsite, as expected, while the alkyl chain and substituted aminophenyl group of these inhibitors fill the +1, +2, and +3 subsites, making hydrophobic and π–π interactions with Phe440, Phe441, and Phe445 that broadly resemble those in the α-GluII–inhibitor structures (Fig. 3). However, to establish these interactions, EB-0150, EB-0176, and EB-0151 must adopt markedly different conformations when bound to α-GluI compared to α-GluII. These

conformations are made possible by the flexibility of the alkyl chain, which we conclude facilitates cross-inhibition by allowing the inhibitors to optimize their interactions with each enzyme. Further studies with α-GluI are in progress to confirm this hypothesis.

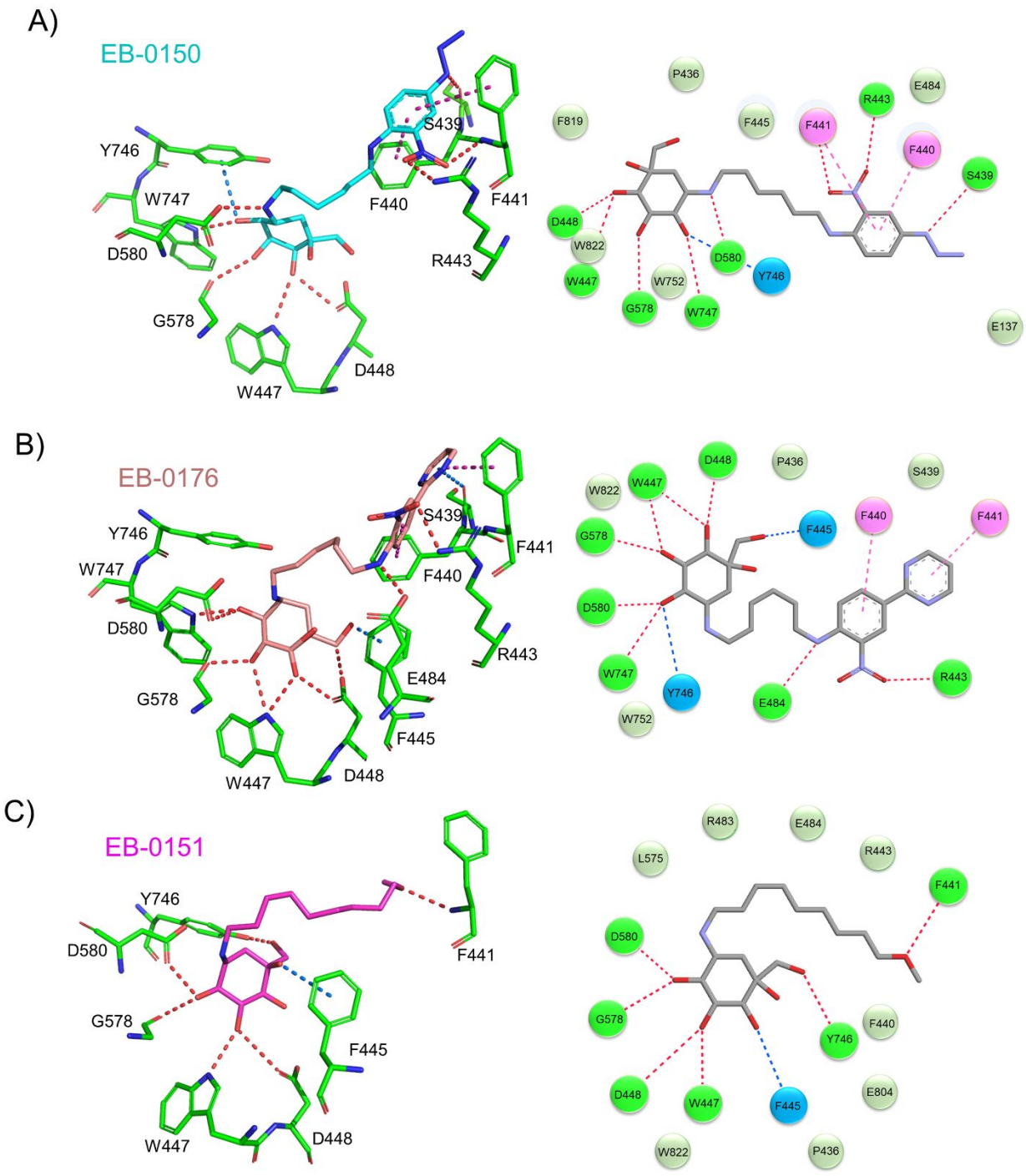

Figure 7. Computational docking of valiolamine-based inhibitors into the active site of ER α-GluI. (A) Interaction of EB-0150 with α-GluI (PDB accession code 5MHF)[31]. Contacting residues of α-GluI are drawn as green sticks. The EB-0150 inhibitor is cyan. Conventional hydrogen bonds

are depicted as red dotted lines, O–H···π hydrogen bonds as blue dotted lines, and π–π interactions as magenta dotted lines. (right) Schematic representation of α-GluI–EB-0150 interactions. Active site residues forming conventional or O–H···π hydrogen bonds are shown as dark green or blue balls, respectively. Residues making π–π interactions or van der Waals contacts with EB-0150 are magenta or light green balls, respectively. (B) (left) Interaction of EB-0176 (salmon) with α-GluI. (right) Schematic representation of α-GluI–EB-0176 interactions. (C) (left) Interaction of EB-0151 (salmon) with α-GluI. (right) Schematic representation of α-GluI–EB-0151 interactions.

***In Vitro* Activity of Valiolamine Derivatives against Dengue Virus (DENV) and SARS-CoV-2**. The antiviral activity of valiolamine and 10 *N*-alkylated derivatives against DENV serotype 2 (DENV2) was assessed in Vero cells using an infectious virus yield reduction assay[28]. The IC_{50} and cell cytotoxicity (CC_{50}) values for individual inhibitors are shown in Table 2. The IC_{50} values ranged from >>1000 μM for UV-0155 (valiolamine) to 1.4 μM for EB-0150, thereby demonstrating the effectiveness of *N*-alkylation. For comparison, IC_{50}s ranging from 2.1 μM to 86.5 μM were reported for UV-4, depending on the DENV strain used (25). Selectivity indexes (CC_{50}/IC_{50}) for the three best antivirals were 88.0 (EB-0150), 101.8 (EB-0159), and 6.9 (EB-0156). Anti-DENV2 activity correlated broadly, but imperfectly, with inhibition of isolated α-GluII or α-GluI. For example, for compounds with nitroxide and azide groups but different alkyl chains, the rank order for anti-DENV2 activity matched that for α-GluII inhibitory potency: EB-0150 (1.4 μM/0.034 μM) > EB-0281 (61.4 μM/1.0 μM) > EB-0283 (233.4 μM/37.0 μM) (Tables 1 and 2). We also observed a correlation between anti-DENV2 activity and α-GluII inhibition for EB-0152 and EB-0159, which have a tetrazole or triazole group but the same alkyl chain: EB-0159 (13.5 μM/16 nM) > EB-0152 (>1000 μM/1.42 μM). However, EB-0176, a very potent inhibitor of both

α-GluII (1.1 nM) and α-GluII (0.64 μM), possessed surprisingly weak anti-DENV2 activity (105.4 μM). As numerous other factors are required for inhibition of viral proliferation (including for examples uptake through the cell membrane and accumulation in the ER), it is not surprising that some molecules show deviation from a simple correlation of antiviral activity and α-GluII inhibition.

We tested the ability of valiolamine-based compounds to reduce replication of SARS-CoV-2 England/2/2020 in a human lung epithelial cell line (Calu-3) using a virus yield assay as described[33]. The IC_{50} values ranged from >1000 μM for UV-0155 (valiolamine) to 9.5 μM for EB-0281 (Table 2), again demonstrating a major contribution of *N*-alkylation to antiviral activity. For comparison, an IC_{50} of 24.5 μM was measured for UV-4 (http://sarscov2.assaytracker.net/results/). Some valiolamine derivatives exhibited broadly similar activities against SARS-CoV-2 and DENV2, as might be expected. For example, the IC_{50} of EB-0150 was 12.3 μM against SARS-CoV-2 compared to 1.4 μM against DENV2 (Table 2). Surprisingly, however, other valiolamines displayed very different activities against SARS-CoV-2 relative to DENV2. For example, the IC_{50} of EB-0288 was 53.7 μM against SARS-CoV-2 versus >1000 μM against DENV2, whereas the IC_{50} of EB-0156 was >100 μM against SARS-CoV-2 versus 18.2 μM against DENV2. Such differences in antiviral activity may reflect virus-specific differences in the mechanism of action of ER α-glucosidase inhibitors. In the case of DENV, it is well-established that ER α-glucosidase inhibitors reduce virion production by disrupting glycan processing of viral envelope proteins[12,13]. However, in the case of SARS-CoV (and possibly SARS-CoV-2), ER α-glucosidase inhibitors may instead act mainly by altering glycan processing of angiotensin I-converting enzyme 2, which is the cellular receptor for SARS-CoV spike protein[34].

Table 2. Antiviral Activity of Valiolamine and Valiolamine Derivatives

Compound	Vero CC_{50} (μM)	DENV IC_{50} (μM)	SARS-CoV-2 IC_{50} (μM)
EB-0155	831.00	>>1000	>1000
EB-0149	>>1000	158.30	N.D.
EB-0151	1071	75.93	270.0
EB-0150	121.5	1.38	12.28
EB-0281	1016	61.44	9.48
EB-0283	1750	293.4	N.D.
EB-0288	>1000	>1000	53.7
EB-0152	1360	>1000	N.D.
EB-0156	125.50	18.19	>100
EB-0159	1377.00	13.53	291.9
EB-0176	761.50	105.4	70.0
Miglustat[1]	N.D.	N.D.	45.2

[1]Miglustat (*N*-butyl-deoxynojirimycin) is an iminosugar derivative used as a positive control for anti-SARS-CoV-2 activity.

CONCLUSIONS

Whereas iminosugars based on DNJ have been studied extensively as ER α-glucosidase inhibitors and potential HTAV therapeutics, other glycomimetics are less studied. In this study, we synthesized a set of *N*-alkylated derivatives of the glycomimetic valiolamine and found that some inhibited α-GluI and α-GluII up to 1,500-fold better than the benchmark DNJ-based iminosugar UV-4. Crystal structures of ER α-GluII bound to these valiolamine derivatives revealed that they achieved their inhibitory potency by occupying all four subsites of the enzyme active site. Moreover, our best derivatives were at least as effective as UV-4 against DENV and SARS-CoV-2 *in vitro*. These findings establish valiolamines as likely inhibitors of the ERQC machinery, and support further investigation of these glycomimetics as broad-spectrum antivirals in animal models.

Scheme 1: Synthesis of *N*-Alkyl Valiolamines[a]

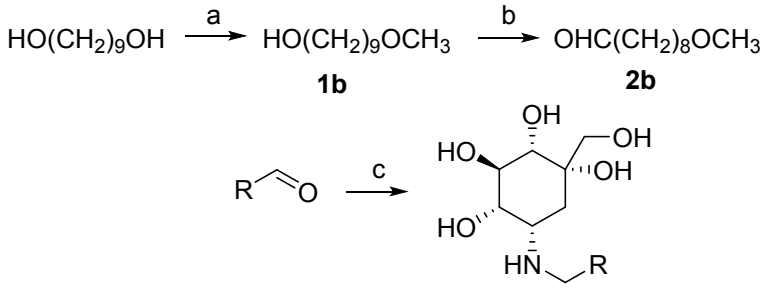

0149: R = $CH_3(CH_2)_2$; 0151: R = CH_3-O-$(CH_2)_8$

a: Reagents and Conditions: (a) (i) HBr, toluene 0-10°C → 85-90°C, 3-3.5hr (ii) NaOMe, MeOH 10-15°C → 65-70°C, 3-4hr (b) DCM, $NaHCO_3$, TEMPO, NaI, NaOCl, 10-15°C → 15-20°C 1-1.5hr (c) Valiolamine, MeOH, AcOH, 10% Pd/C, H_2, rt 16hr.

Scheme 2: Synthesis of *N*-Aralkyl Valiolamines[a]

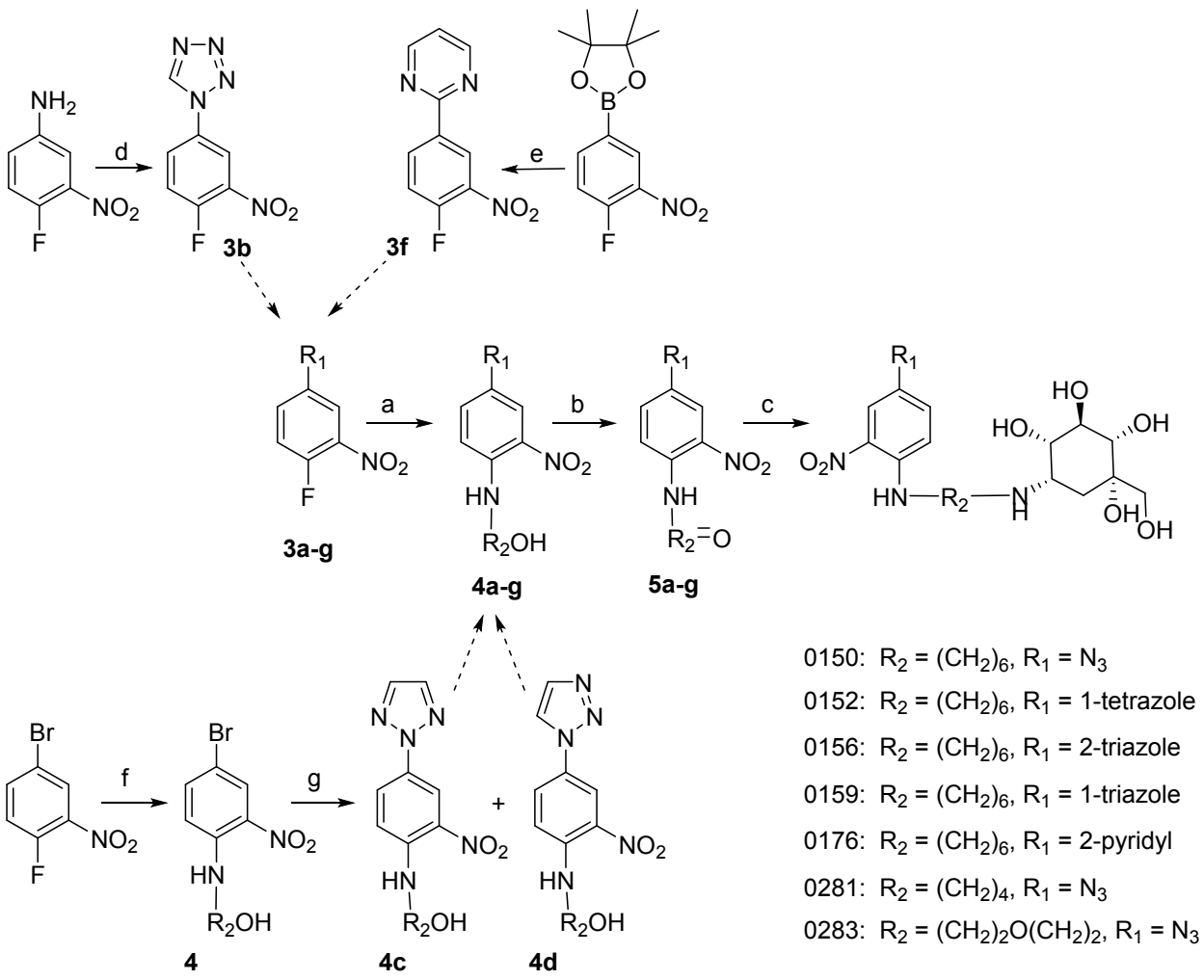

a: Reagents and Conditions: (a) 1,4-dioxane, TEA, 55°C under N_2 atmosphere, 16 hrs; (b) DCM, DMP, 0°C → rt, 2 hrs; or THF, $(COCl)_2$, DMSO, -78°C, 2 hrs, TEA (EB-0176); or DCM, $(COCl)_2$, DMSO, -78°C, 2 hrs, TEA (EB-0283) (c) MeOH, valiolamine, AcOH, $NaCNBH_3$, rt, 16 hrs; (d) (EB-0152) triethylorthoformate, trimethylsilyl azide, 0°C → 80°C, 4 hrs; (e) (EB-0176) 1:1:1 EtOH:toluene:water, 2-bromopyrimidine, Na_2CO_3, $Pd(dppf)_2Cl_2$, 80°C, 4 hrs; (f) 1,4-dioxane, TEA, 6-aminohexan-1-ol, 60°C, 16 hrs; (g) 1H-1,2,3-triazole, Cu, K_2CO_3 rt → 160°C, 24 hrs, product mixture purified by flash chromatography with 30% EtOAc/hexane.

Scheme 3: Synthesis of EB-0288[a]

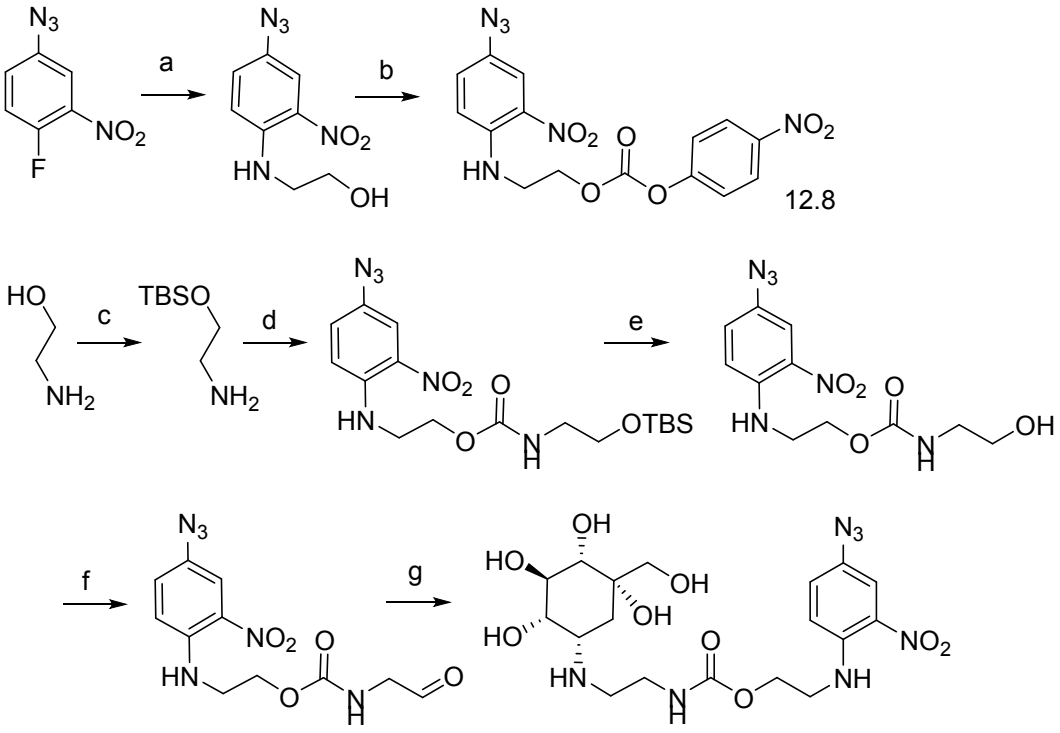

a: Reagents and Conditions: (a) 1,4-dioxane, TEA, 2-aminoethanol, 100°C, 12 hrs; (b) DCM, TEA, 4-nitrophenyl chloroformate, 0°C → rt, 12 hrs; (c) DCM, TBDMS-Cl, rt, 2 hrs; (d) THF, intermediate 12.8, $NaHCO_3$, 100°C in sealed tube, 12 hrs; (e) THF, TBAF, 0°C, 2 hrs; (f) DCM, $(COCl)_2$, DMSO, -78°C, 4 hrs; (g) MeOH, valiolamine, $NaCNBH_3$, rt, 12 hrs

EXPERIMENTAL SECTION

General Procedures. All solvents and chemicals were used as purchased without further purification. Reactions were monitored by thin layer chromatography on silica gel 60 on aluminium sheets (Merck Life Science Private Limited) and exposed under UV (long UV 365 nm and short UV 254 nm). The reaction mixtures were filtered and the filtrates concentrated under vacuum. Initial purification was by silica gel chromatography (100–200 or 60–120 mesh) with hexane/ethyl acetate mixtures. Preparative HPLC purification using KINETEX Evo reverse phase C18 column (5 μm, 250 mm × 21.2 mm), with a water/acetonitrile gradient and 5 mM ammonium bicarbonate buffer, followed by solvent evaporation and/or freeze drying, provided the target molecules with the indicated purity (>95%). Proton (^{1}H) NMR spectra were recorded on a Bruker Avance III 400 or a Varian Unity Inova 500 using CD_3OD as solvent. Chemical shifts are given in parts per million (400 MHz/500 MHz) relative to tetramethylsilane. Purity by HPLC was determined on a Shimadzu LC-2010 CHT instrument with PDA detector or Agilent 1200 Series instrument with PDA detector. The column was a C18 column such as Eclipse XBD (150 x 4.6mm, 5 micron) or X-select CSH (150 x 4.6 mm, 3.5 μm), gradient was mobile phase A: 0.05% TFA in water or 5 mM NH_4HCO_3 in water, mobile phase B: acetonitrile (ACN), example program (time/%B): 0.01/20, 3/20, 10/90, 20/90, flow rate 1.0 mL/min.

Materials. All syntheses followed a similar scheme where the optionally-substituted alkylene moiety and (as relevant) the aryl ring system were prepared following methodologies previously reported (WO-2010096764-A1, US-20180273473-A1, WO-2016073652-A1, application 62/705,698) with a primary hydroxyl on the alkylene. The hydroxyl was then oxidized to aldehyde using either Swern conditions or Dess–Martin Periodinane, followed by a one-pot reductive amination coupling to commercially purchased valiolamine. Reductive aminations used either

hydrogen gas with 10% Pd/C catalyst (EB-0149, EB-0151) or 1.5 eq sodium cyanoborohydride (all other targets).

(1S,2S,3R,4S,5S)-5-(butylamino)-1-(hydroxymethyl)cyclohexane-1,2,3,4-tetraol (EB-0149). Colorless thick syrup, 19% yield after HPLC purification, 99.97% purity by LC with mass-selective detection; expected mass 249.3, observed MH+ 250.2; ^{1}H-NMR (500 MHz, CD_3OD): δ 3.79-3.75 (m, 1H), 3.60-3.51 (m, 2H), 3.37-3.35 (m, 2H), 3.30-3.21 (m, 1H), 2.99-2.94 (m, 1H), 2.69-2.63 (m, 1H), 2.08-2.03 (m, 1H), 1.62-1.55 (m, 3H), 1.42-1.35 (m, 2H), 0.89 (t, 3H).

(1S,2S,3R,4S,5S)-5-((6-((4-azido-2-nitrophenyl)amino)hexyl)amino)-1-(hydroxymethyl)cyclohexane-1,2,3,4-tetraol (EB-0150) Orange-red solid, 22% yield after HPLC purification, 99.50% purity by HPLC; expected mass 454.4, observed MH+ 455.4; NMR (400 MHz, CD_3OD): δ 7.80 (d, J = 2.7 Hz, 1H), 7.26 (dd, J = 9.2, 2.8 Hz, 1H), 7.09 (d, J = 9.2 Hz, 1H), 3.75-3.67 (m, 1H), 3.57-3.48 (m, 2H), 3.40 -3.37 (m, 2H), 3.36 (t, J = 1.6 Hz, 1H), 3.12-3.06 (m, 1H), 2.85-2.77 (m, 1H), 2.57 - 2.45 (m, 1H), 2.01 (dd, J = 15.0, 3.2Hz, 1H), 1.78-1.69 (m, 2H), 1.62-1.39 (m, 8H).

(1S,2S,3R,4S,5S)-1-(hydroxymethyl)-5-((9-methoxynonyl)amino)cyclohexane-1,2,3,4-tetraol (EB-0151). Colorless thick syrup, 23% yield after HPLC purification, 99.88% purity by HPLC; expected mass 349.4, observed MH+ 350.3; NMR (500 MHz, CD3OD): δ 3.75 (t, 1H), 3.59-3.51 (m, 2H), 3.39-3.35 (m, 4H), 3.34-3.31 (m, 4H), 3.10-3.05 (m,1H), 2.80-2.75 (m, 1H), 2.71-2.65 (m, 1H), 2.01 (dd, 1H), 1.49-1.41 (m, 5H), 1.39-1.31 (m, 9H). Elemental analysis calculated (%) for C17H35NO6: C 58.43, H 10.1, N 4.01. Found: C 60.14, H 9.82, N 3.96.

(1S,2S,3R,4S,5S)-1-(hydroxymethyl)-5-((6-((2-nitro-4-(1H-tetrazol-1-yl)phenyl)amino)hexyl)amino)cyclohexane-1,2,3,4-tetraol (EB-0152). Yellow thick syrup, 16% yield after HPLC purification, purity by HPLC 99.59%; expected mass 481.5, observed MH+ 482.4; NMR (500 MHz, CD_3OD): δ 9.75 (s, 1H), 8.62 (d, 1H), 7.99-7.90 (m, 1H), 7.25 (d, 1H), 3.79-3.75 (m, 2H), 3.59-3.49 (m, 4H), 3.39-3.35 (m, 2H), 3.10-3.05 (m,1H), 2.80-2.75 (m, 1.6H), 2.71-2.65 (m, 1.4H), 2.01 (dd, 1H), 1.82-1.75 (m, 2H), 1.61-1.43 (m, 6H).

(1S,2S,3R,4S,5S)-1-(hydroxymethyl)-5-((6-((2-nitro-4-(2H-1,2,3-triazol-2-yl)phenyl)amino)hexyl)amino)cyclohexane-1,2,3,4-tetraol (EB-0156). Orange solid, 26% yield after HPLC purification, 99.19% purity by HPLC; expected mass 480.5, observed MH+ 481.4; NMR (500 MHz, CD3OD): δ 8.79 (s, 1H), 8.32-8.21 (m, 1H), 7.91 (s, 2H), 7.21 (dd, 1H), 3.75 (t, 1H), 3.59-3.51 (m, 2H), 3.39-3.35 (m, 2H), 3.34-3.31 (m, 2H), 3.10-3.05 (m, 1H), 2.85-2.80 (m, 1H), 2.59-2.51 (m 1H), 2.01 (dd, 1H), 1.82-1.75 (m, 2H), 1.61-1.42 (m, 7H). Elemental analysis calculated (%) for C21H32N6O7: C 52.49, H 6.71, N 17.49. Found: C 51.63, H 6.55, N 17.10.

(1S,2S,3R,4S,5S)-1-(hydroxymethyl)-5-((6-((2-nitro-4-(1H-1,2,3-triazol-1-yl)phenyl)amino)hexyl)amino)cyclohexane-1,2,3,4-tetraol (EB-0159). Orange-red solid, 28% yield after HPLC purification, 95.01% purity by HPLC, 98.74% purity by LCMS; expected mass 480.5, observed MH+ 481.1; NMR (400 MHz, CD_3OD): δ 8.57 (d, J = 2.7 Hz, 1H), 8.49 (d, J = 1.0 Hz, 1H), 7.99 (dd, J = 9.3, 2.7 Hz, 1H), 7.88 (d, J = 1.1 Hz, 1H), 7.24 (d, J = 9.4 Hz, 1H), 3.72 (t, J = 9.8 Hz, 1H), 3.57-3.43 (m, 4H), 3.40-3.32 (m, 1.93H), 3.12-3.04 (m, 1H), 2.85-2.75 (m, 1.13H), 2.53-2.45 (m, 1.03H), 2.00 (dd, J = 14.9, 3.2 Hz, 1.02H), 1.82-1.73 (m, 1.99H), 1.60-1.42 (m, 7.12H).

(1S,2S,3R,4S,5S)-1-(hydroxymethyl)-5-((6-((2-nitro-4-(pyrimidin-2-yl)phenyl)amino)hexyl)amino)cyclohexane-1,2,3,4-tetraol (EB-0176). Orange solid, yield 80% after HPLC purification, 95.73% purity by HPLC; 100.0% purity by LCMS; expected mass 491.5, observed MH+ 492.3; NMR (400 MHz, CD3OD): δ 9.23 (d, J = 2.1 Hz, 1H), 8.78 (d, J = 4.9 Hz,

2H), 8.52 (dd, J = 9.2, 2.1 Hz, 1H), 7.28 (t, J = 4.8 Hz, 1H), 7.14 (d, J = 9.2 Hz, 1H), 3.75-3.69 (m, 1H), 3.56-3.50 (m, 2H), 3.49-3.43 (m, 2H), 3.39-3.35 (m, 1H), 3.14-3.08 (m, 1H), 2.92-2.71 (m, 1H), 2.60-2.43 (m, 1H), 2.02 (dd, J = 15.0, 3.2 Hz, 1H), 1.82-1.73 (m, 2H), 1.65 - 1.38 (m, 7H).

(1S,2S,3R,4S,5S)-5-((5-((4-azido-2-nitrophenyl)amino)pentyl)amino)-1-(hydroxymethyl)cyclohexane-1,2,3,4-tetraol (EB-0281). Orange-red viscous syrup, yield 38% after HPLC purification, 98.02% purity by HPLC; 99.72% purity by LCMS; expected mass 426.4, observed masses 427.1 (M+H+), 449.2 (M+Na+); NMR (400 MHz, CD_3OD): δ 7.81 (d, J = 2.8 Hz, 1H), 7.28 (dd, J = 9.3, 2.8 Hz, 1H), 7.12 (d, J = 9.3 Hz, 1H), 3.78-3.69 (m, 1H), 3.66-3.59 (m, 1H), 3.56 (d, J = 10.9 Hz, 1H), 3.49-3.42 (m, 2H), 3.42-3.37 (m, 2H), 3.21-2.99 (m, 2H), 2.95-2.76 (m, 1H), 2.15-2.09 (m, 1H), 1.86-1.72 (m, 4H), 1.71-1.62 (m, 1H).

(1S,2S,3R,4S,5S)-5-((2-(2-((4-azido-2-nitrophenyl)amino)ethoxy)ethyl)amino)-1-(hydroxymethyl)cyclohexane-1,2,3,4-tetraol (EB-0283). Orange red solid, yield 45% after HPLC purification; 98.18% purity by HPLC; 99.22% purity by LCMS; expected mass 442.4, observed mass 443.2 (M+H+), 465.1 (M+Na+); NMR (400 MHz, CD_3OD): δ 8.24 (br s, 1H), 7.80 (d, J = 2.6 Hz, 1H), 7.27 (dd, J = 9.3, 2.8 Hz, 1H), 7.14 (d, J = 9.3 Hz, 1H), 3.80-3.71 (m, 3H), 3.70 -3.63 (m, 1H), 3.63-3.49 (m, 5H), 3.38-3.36 (m, 1H), 3.34 (d, J = 4.3 Hz, 1H), 3.13-3.08 (m, 1H), 2.98-2.90 (m, 1H), 2.75-2.67 (m, 1H), 2.01 (dd, J = 15.1, 3.3Hz, 1H), 1.47 (dd, J = 2.7, 15.0 Hz, 1H).

2-((4-azido-2-nitrophenyl)amino)ethyl (2-(((1S,2S,3R,4S,5S)-2,3,4,5-tetrahydroxy-5-(hydroxymethyl)cyclohexyl)amino)ethyl)carbamate (EB-0288). Red semi-solid, yield 17% after HPLC purification, 99.31% purity by HPLC; 97.83% purity by LCMS; expected mass 485.4, observed MH+ 486.4; NMR (400 MHz, CD_3OD): δ 7.81 (d, J = 2.6 Hz, 1H), 7.28 (dd, J = 9.2, 2.7 Hz, 1H), 7.21-7.13 (m, 1H), 4.37-4.24 (m, 2H), 3.76- 3.59 (m, 3H), 3.56-3.43 (m, 2H), 3.37-3.33 (m, 2H), 3.28-3.16 (m, 2H), 3.09-3.06 (m, 1H), 2.90-2.82 (m, 1H), 2.62-2.54 (m, 1H), 2.09-1.86 (m, 1H), 1.57-1.37 (m, 1H).

Preparation of Human ER α-Glucosidase I for Enzyme Inhibition Assays. The amino acid sequence for full-length human α-GluI was obtained from UniProt (Q13724). Constructs were cloned into Gateway Entry vector (ThermoFisher) consisting of the full-length open reading frame (ORF) preceded by a Kozac sequence and His_6 affinity tag at the C-terminus. The entry vector was cloned into BacMam Destination vector (Kemp Proteins) and transformed into chemically competent DH10Bac *E. coli* cells to produce recombinant α-GluI bacmids. Bacmid isolates were obtained following two rounds of blue-white screening and were transfected into Sf9 cells cultivated in serum-free medium (ThermoFisher). At 4 days' post-transfection, culture supernatants containing virus were harvested and filter-sterilized. The virus titer was determined using a plaque assay on Sf9 cell monolayers and expressions were performed using HEK293T cells cultivated in Freestyle 293 medium (ThermoFisher) at a multiplicity of infection (MOI) of 4. Soluble human α-GluI was detected by anti-His western blots in the soluble cell extract following extraction with 1% (v/v) NP40 for 30 min at 0°C. Production of α-GluI at the 10 L scale was performed in stirred-tank bioreactors at 27°C and 80 rpm with dissolved oxygen level at 50% oxygen in air and pH 7.0–7.2. Cells were transduced at MOI of 4 and the cell pellet was harvested at 48 h post-transduction. The pellet was lysed by resuspension in 1 L of 50 mM $NaH_2PO_4.H_2O$, 300 mM NaCl, 10 mM imidazole, 1 mM phenylmethylsulfonyl fluoride, and 1% (v/v) NP40 (pH 8.0). The suspension was incubated on ice for 30 min and then centrifuged at 20,000 × g. The lysate was loaded onto a Ni-NTA Superflow (Qiagen) column. Bound α-GluI was eluted using a linear gradient of 0–60% 50 mM $NaH_2PO_4.H_2O$, 300 mM NaCl, and 500 mM imidazole (pH 8.0). Fractions containing human α-GluI were pooled and dialyzed into storage buffer (20 mM Tris-HCl, 300 mM NaCl, 50 mM L-arginine, 10 mM EDTA, and 0.01% (v/v) Tween 80 (pH 7.5)).

Preparation of Mouse ER α-Glucosidase II for Enzyme Inhibition Assays. To produce full-length mouse α-GluII, a single construct was designed for each of the α and β subunits for cloning into Gateway Entry vectors. The α subunit was appended with a streptavidin tag and the β subunit with a His_6 tag. The entry vectors were cloned into BacMam Destination vectors and the vectors were transformed into DH10Bac *E. coli* cells to produce recombinant α-GluII bacmids. Bacmid isolates for each of the subunits were obtained following two rounds of blue-white screening and were then transfected into Sf9 cells cultivated in serum-free medium (ThermoFisher). MOI of 10 with a ratio of 75% α subunit and 25% β subunit was selected for expression. Production of mouse α-GluII at the 10 L scale was performed in stirred-tank bioreactors at 27 °C and 80 rpm with dissolved oxygen level at 50% of oxygen in air and pH 7.0–7.2. Cells were transduced at MOI of 10 and the cell pellet was harvested at 48 h post-transduction. The supernatant was stirred overnight at 4°C with Nickel-Sepharose Excel resin (GE Healthcare). The resin was collected into a column and washed with 2X Dulbecco's PBS (pH 7.4). Bound α-GluII protein was eluted using a linear gradient of 0–60% 2X Dulbecco's PBS and 500 mM imidazole (pH 7.4). Fractions containing α-GluII heterodimers were pooled and concentrated. The protein was further purified using a Superdex 200 column (GE Healthcare) equilibrated with PBS (pH 7.2).

Inhibition of ER α-GluI and α-GluII Activity *In Vitro*. The α-GluI inhibition assay was performed by incubating purified recombinant human α-GluI with multiple dilutions of test compounds for 60 min at 37°C. A synthetic trisaccharide substrate analog (compound 9)[35] was then added to the mixture for 90 min at 37°C. The reaction was stopped with 1.5 M Tris (pH 8.0). In the absence of inhibition, the terminal glucose of the trisaccharide substrate is hydrolyzed by the enzyme, releasing glucose, which is measured *via* a reporter reaction. The D-glucose product

was detected using Amplex Red Glucose/Glucose Oxidase Assay Kit (Invitrogen), where glucose oxidase reacts with D-glucose to form D-gluconolactone and H_2O_2, which then reacts with the Amplex Red reagent to generate a red-fluorescent oxidation product (560 nm, excitation; 590 nm, emission). The lower signal was correlated with α-GluI inhibition. Percent inhibition was plotted as a function of concentration for each compound, compared to control reactions. The 50% inhibitory capacity (IC_{50}) was determined using a 4-PL curve fit and serves as a measure of relative inhibitory activity of each test compound.

The α-GluII inhibition assay was performed by incubating purified recombinant mouse α-GluII for 60 min at 37°C with multiple dilutions of test compounds. 4-methylumbelliferyl-α-D-pyranoside was then introduced as the substrate to the mixture. Fluorogenic 1,4-methyllumbelliferone was generated, and the reaction was stopped with 0.5 M glycine and 0.3 M NaOH (pH 10) after an incubation of 30 min at 37°C. 1,4-methyllumbelliferone was detected by fluorescence (excitation at 365 nm, emission at 440 nm). Percent inhibition was plotted as a function of concentration for each test compound. The IC_{50} was determined using a 4-PL curve fit.

In each set of glucosidase inhibition assays, three reference substances (DNJ, UV-4, and UV-5) were included as low, moderate, and highly inhibitory controls respectively, to confirm performance of the assay. The average IC_{50} values for each reference substance against each enzyme are: α-GluI IC_{50}: 14.94, 0.50, 0.13 μM, and α-GluII IC_{50}: 11.39, 0.11, 0.02 μM, for DNJ, UV-4, and UV-5, respectively.

***In Vitro* Assessment of Activity against Dengue Virus.** Vero cells were used for testing the antiviral activity and cytotoxicity of the compounds[28]. To measure cytotoxicity, the Cell Titer-Glo Luminescent Cell Viability Assay (Promega) was used. Compounds were tested at 6–8

concentrations in three replicates. Vehicle-only treated cells were used as control with 100% surviving cells, DMSO-killed cells as a cell death-inducing control, and no cells for 0% surviving cells. Cytotoxicity was measured 3–5 days after incubation with test compounds by the change/decrease in relative light units in each sample, which reflects the amount of ATP present (an indicator of metabolically active cells). The 50% cellular cytotoxicity (CC_{50}) value was calculated based on the relative light units of the compound-treated samples using vehicle-only control as 100% survival and no cells as 0% survival.

To test the ability of the compounds to reduce viral replication, a virus yield assay was performed[25]. Supernatant samples generated from virus-infected Vero cells incubated with different concentrations of each compound were subsequently enumerated using a standard plaque assay. The compounds were tested at 6 concentrations against dengue virus (DENV serotype 2, strain New Guinea C). In the yield assay, the concentrations started at 125 μM with 2-fold dilutions. Each concentration was tested in duplicate. The diluted compounds were added to cells 1 h prior to infection. After 5 days, supernatants were harvested and analyzed for virus content using plaque assay. For the plaque assay, Vero cells were seeded in 24-well plates and allowed to adhere overnight. The next day each of the harvested supernatants from the yield-reduction assay were serially diluted up to 10-fold, growth medium was removed, and cells were infected with the dilutions of the supernatants. After 1 h, 0.8% methylcellulose was added without removal of the inoculum. The plates were incubated for 4 days, cells fixed and permeabilized in 80%/20% (v/v) mixture of ethanol and methanol. The resulting cells were incubated for 1 h with DENV E-specific antibody (monoclonal antibody 4G2, obtained from ATCC). After washing, a secondary HRP-conjugated goat anti-mouse antibody was added and incubated for 1 h. Foci of viral infection were visualized with an insoluble peroxidase substrate (TrueBlue) and plaques counted. A 4PL curve

was used to generate IC_{50} values based on percent reduction of virus yield compared to a wild-type titer (no compound control) and these were calculated using XLFit equation 205.

***In Vitro* Assessment of Activity against SARS-CoV-2.** A virus yield assay was performed as described[33] to test the ability of compounds to reduce replication of SARS-CoV-2 England/2/2020 in Calu-3 human lung epithelial cells, followed by a focus forming assay in Vero cells to quantify Calu-3 secreted virions.

Expression and Purification of Mouse ER α-Glucosidase II for Crystallization. Codon-optimized genes encoding the α and β chains of mouse ER α-GluII were synthesized and cloned into the mammalian expression vector pcDNA3.4 TOPO (GenScript). Both genes included an N-terminal signal sequence (MGILPSPGMPALLSLVSLLSVLLMGCVAETG)[36] for secretion. The β chain also included a C-terminal His_6 tag for affinity purification. The C-terminal ER retention signal (KDEL) of the β chain was omitted to allow secretion of α-GluII into the culture medium. In addition, the Asn97 of the α chain was mutated to aspartate to eliminate an *N*-glycosylation site.

The α-GluII α and β chain constructs were transfected at a 1:1 mass ratio into Expi293F cells using Expifectamine293 (ThermoFisher) following the manufacturer's protocol. Cells were grown at 37°C, 8% CO_2, and 125 rpm. After 72 h, cells were harvested by centrifugation at 11,000 × g for 10 min. The supernatant was dialyzed against PBS overnight at 4°C, then loaded onto a TALON IMAC column charged with Co^{2+} (Takara). Recombinant α-GluII was eluted using a 0–400 mM imidazole gradient. Eluted fractions were concentrated with a 10 kDa molecular weight cut-off Amicon Ultra-15 ultrafiltration device (Millipore). The protein was further purified using

a Superdex 200 column (GE Healthcare) equilibrated with 50 mM Tris-HCl (pH 8.0) and 150 mM NaCl. The yield of α-GluII was typically 3 mg/L of culture.

For crystallization, full-length α-GluII (1 mg/mL) was treated for 4 h at 30°C with sequencing grade modified trypsin (Promega), supplemented with 2 mM $CaCl_2$, at a 1:100 trypsin:α-GluII mass ratio. Trypsinized α-GluII (α-$GluII_{Tryp}$) was purified on a Superdex 200 column equilibrated with 20 mM HEPES (pH 7.5) and 100 mM NaCl.

Crystallization and Data Collection. Apo α-$GluII_{Tryp}$ was concentrated to 7.5 mg/mL for crystallization trials. Diamond-shaped crystals were obtained at room temperature by sitting drop vapor diffusion in 0.09 M NPS (0.03 M sodium nitrate, 0.03 sodium phosphate dibasic, and 0.03 M ammonium sulfate), 0.1 M Buffer System 1 (pH 7.0), and 29% (v/v) P500MME P20K (Morpheus MD 1-47 Kit; Molecular Dimensions). Streak seeding was used to increase crystal size. The crystals were cross-linked with 25% (v/v) glutaraldehyde for 10 min. Inhibitors were first dissolved in DMSO then diluted in reservoir solution prior to soaking crystals for complex formation. Apo α-$GluII_{Tryp}$ crystals were transferred to drops containing inhibitors at concentrations ranging from 100 μM to 1 mM and soaked for 1 to 3 days before freezing in liquid nitrogen in the presence of 15% (v/v) ethylene glycol. X-ray diffraction data for all α-$GluII_{Tryp}$–inhibitor complexes except α-$GluII_{Tryp}$–EB-0150 were collected at beamline 23-ID-B of the Advanced Photon Source, Argonne National Laboratory. Data for α-$GluII_{Tryp}$–EB-0150 were collected at beamline 19-BM-D. Diffraction data were indexed, integrated, and scaled using the program HKL2000[37]. The data were processed in space group $P3_2$ with unit cell parameters $a = b$ = 103.0 Å, c = 240.6 Å, α = β = 90°, and γ = 120°. The soaked crystals diffracted from 2.07 Å to 2.55 Å resolution. Data collection statistics are shown in Supplementary Table 1.

Structure Determination and Refinement. Structures of α-GluII$_{Tryp}$–inhibitor complexes were determined by molecular replacement using the program Phaser[38] with apo α-GluII$_{Tryp}$ (PDB accession code 5F0E)[25] as the search model. After an initial cycle of rigid body refinement, the models were built manually in Coot[39] and refined with Phenix[40]. The inhibitors were modeled into unambiguous $F_o - F_c$ electron density observed in the α-GluII$_{Tryp}$ active site. The restrain files for inhibitors were generated using ReadySet[41,42]. Refinement statistics are summarized in Supplementary Table 1. Interactions were calculated with Discovery Studio (https://www.discngine.com/discovery-studio). The program PyMOL (https://pymol.org/2/) was used to prepare figures.

Computational Docking. Three representative *N*-substituted valiolamine derivatives (EB-0150, EB-0176 and EB-0151) were selected for docking into the active site of ER α-GluI using the automated molecular docking software AutoDock4[32,43]. The crystal structure of mouse ER α-GluI in complex with the iminosugar UV-4B[31] was retrieved from the PDB (accession code 5MHF). The macromolecule and ligands were prepared using AutoDockTools4[32]. The size of the grid box was 60 Å × 60 Å × 60 Å. Docking calculations were carried out by default values (100 runs, population size of 150, total number of evaluations 5,000,000 generations, default value of 0.8 for crossover rate, mutant rate of 0.02). All results for each ligand were analyzed in AutoDockTools4. The top 10 conformations were chosen for analysis.

ACKNOWLEGDMENTS

This work was supported by a Sponsored Research Agreement between the University of Maryland and Emergent BioSolutions. J.L. Kiappes is a Lerner–Fink Fellow. MLH, JLK, and NZ acknowledge the philanthropic support of the donors to the University of Oxford's COVID-19 Research Response Fund. Recombinant proteins for enzyme assays were produced by Kemp Proteins (Frederick, MD). We thank Mr. Sreenivasa Rao Vemur (Sai Life Sciences, Hyderabad, India) for assistance with chemical syntheses. Enzyme inhibition and dengue antiviral assays were performed by IBT Bioservices (Rockville, MD). Crystallographic results are based on X-ray data collected at both Structural Biology Center and GM/CA beamlines at the Advanced Photon Source of Argonne National Laboratory, operated by UChicago Argonne, LLC, for the U.S. Department of Energy, Office of Biological and Environmental Research under contract DE-AC02-06CH11357.

ANCILLARY INFORMATION

Supporting Information Availability. Supporting Information includes current author affiliations, a CSV file which includes molecular formula strings, and analytical data (calculated and observed mass, proton NMR, chromatograms, mass spectra).

PDB ID of New Crystal (X-ray) Structures. Atomic coordinates and structure factors have been deposited in the Protein Data Bank under accession codes 7JT (α-GluII+EB-0149), 7KR (α-GluII+EB-0150), 7K9N (α-GluII+EB-0151), 7K9O (α-GluII+EB-0152), 7K9Q (α-GluII+EB-0155), 7K9T (α-GluII+EB-0156), 7KAD (α-GluII+EB-0159), 7KB6 (α-GluII+EB-0176), 7KB8 (α-GluII+EB-0281), 7KBJ (α-GluII+EB-0283), 7KBR (α-GluII+EB-0288), and 7L9E (apo α-GluII). Authors will release the atomic coordinates and experimental data upon article publication.

Corresponding Author Information. Roy A. Mariuzza (rmariuzz@umd.edu)

Abbreviations Used. α-GluI, α-glucosidase I; α-GluII, α-glucosidase II; DAAs, direct-acting antiviral agents; DENV, dengue virus; DNJ, 1-deoxynojirimycin ((2R,3R,4R,5S)-2-(hydroxymethyl)piperidine-3,4,5-triol); ER, endoplasmic reticulum; ERQC, endoplasmic reticulum quality control; HCV, hepatitis C virus; HTAV(s), host-targeted antiviral agent(s); LDLRa, low-density lipoprotein receptor class A; MGAM, maltase-glucoamylase; MOI, multiplicity of infection; SARS-CoV-2, severe acute respiratory syndrome coronavirus 2; SI, sucrase-isomaltase.

Author Contributions. SSK, MLH, JLK, RM, and BA performed the experiments and data analyses. NZ, KLW, AMT, and RAM conceived and supervised the project. SSK, AMT, and RAM wrote the manuscript.

REFERENCES

1. Ji, X.; Li, Z.; Medicinal chemistry strategies toward host targeting antiviral agents. *Med. Res. Rev.* **2020,** 40, 1519-1557.
2. Poveda, E.; Wyles, D. L.; Mena, A.; Pedreira, J. D.; Castro-Iglesias, A.; Cachay, E. Update on hepatitis C virus resistance to direct-acting antiviral agents. *Antiviral Res.* **2014**, 108, 181-191.
3. Hayes, C. N.; Chayama, K. Why highly effective drugs are not enough: the need for an affordable solution to eliminating HCV. *Expert Rev. Clin. Pharmacol.* **2017,** 10, 583-594.
4. Wisskirchen, K.; Lucifora, J.; Michler, T.; Protzer, U. New pharmacological strategies to fight enveloped viruses. *Trends Pharmacol. Sci.* **2014,** 35**,** 470-478.
5. Martinez, J. P.; Sasse, F.; Brönstrup, M.; Diez, J.; Meyerhans, A. Antiviral drug discovery: broad-spectrum drugs from nature. *Nat. Prod. Rep*. **2015,** 32, 29-48.
6. Wang, Y.; Jin, F.; Wang, R.; Li, F.; Wu, Y.; Kitazato, K.; Wang, Y. HSP90: a promising broad-spectrum antiviral drug target. *Arch Virol.* **2017,** 162, 3269-3282.
7. Pieren, M.; Galli, C.; Denzel, A.; Molinari, M. The use of calnexin and calreticulin by cellular and viral glycoproteins. *J. Biol. Chem*. **2005,** 280, 28265-28271.
8. Hammond, C.; Braakman, I.; Helenius, A. Role of N-linked oligosaccharide recognition, glucose trimming, and calnexin in glycoprotein folding and quality control. *Proc. Natl. Acad. Sci. USA* **1994,** 91, 913-917.
9. Dalziel, M.; Crispin, M.; Scanlan, C. N.; Zitzmann, N.; Dwek, R.A. Emerging principles for the therapeutic exploitation of glycosylation. *Science* **2014,** 343, 1235681.
10. D'Alessio, C.; Caramelo, J. J.; Parodi, A. J. UDP-GlC:glycoprotein glucosyltransferase-glucosidase II, the ying-yang of the ER quality control. *Semin. Cell Dev. Biol*. **2010,** 21, 491-499.
11. Ruddock, L. W.; Molinari, M. N-glycan processing in ER quality control. *J. Cell Sci.* **2006**, 119, 4373-4380.
12. Chang, J.; Block, T. M.; Guo, J. T. Antiviral therapies targeting host ER alpha-glucosidases: current status and future directions. *Antiviral Res*. **2013,** 99, 251-260.
13. DeWald, L. E.; Starr, C.; Butters, T.; Treston, A.; Warfield, K. L. Iminosugars: a host-targeted approach to combat *Flaviviridae* infections. *Antiviral Res.* doi: 10.1016/j.antiviral.2020.104881. Published online: Available online 5 August 2020.
14. Lin, P.; Zeng, J. C.; Chen, J. G.; Nie, X. L.; Yuan, E.; Wang, X. Q.; Peng, D. Y.; & Yin, Z. P. Synthesis, *in vitro* inhibitory activity, kinetic study and molecular docking of novel *N*-alkyl-deoxynojirimycin derivatives as potential α-glucosidase inhibitors. *J. Enzyme Inhib. Med. Chem.* **2020,** 35, 1879-1890.
15. Perry, S. T.; Buck, M. D.; Plummer, E. M.; Penmasta, R. A.; Batra, H.; Stavale, E. J.; Warfield, K. L.; Dwek, R. A.; Butters, T. D.; Alonzi, D. S.; Lada, S. M.; King, K.; Klose, B.; Ramstedt, U.; Shresta, S. An iminosugar with potent inhibition of dengue virus infection in vivo. *Antiviral Res*. **2013**, 98, 35-43.
16. Warfield, K. L.; Alonzi, D. S.; Hill, J. C; Caputo, A. T.; Roversi, P.; Kiappes, J. L.; Sheets, N.; Duchars, M.; Dwek, R. A.; Biggins, J.; Barnard, D.; Shresta, S.; Treston, A. M.; Zitzmann, N. Targeting endoplasmic reticulum α-glucosidase I with a single-dose iminosugar treatment protects against lethal influenza and dengue virus infections. *J. Med. Chem*. **2020,** 63, 4205-4214.

17. Stavale, E. J.; Vu, H.; Sampath, A.; Ramstedt, U.; Warfield, K. L. In vivo therapeutic protection against influenza A (H1N1) oseltamivir-sensitive and resistant viruses by the iminosugar UV-4. *PLoS One* **2015,** 10, e0121662.
18. Warfield, K. L.; Barnard, D. L.; Enterlein, S. G.; Smee, D. F.; Khaliq, M.; Sampath, A.; Callahan, M. V.; Ramstedt, U.; Day, C. W. The iminosugar UV-4 is a broad inhibitor of influenza A and B viruses ex vivo and in mice. *Viruses* **2016**, 8, 71-79.
19. Williams, S. J.; Goddard-Borger, E. D. α-glucosidase inhibitors as host-directed antiviral agents with potential for the treatment of COVID-19. *Biochem. Soc. Trans*. **2020,** 48, 1287-1295.
20. Clark, E. C.; Nofchissey, R. A.; Ye, C.; Bradfute, S. B. The iminosugars celgosivir, castanospermine and UV-4 inhibit SARS-CoV-2 replication. *Glycobiology* **2021**, 31, 378-384.
21. Dhameja, M.; Gupta, P. Synthetic heterocyclic candidates as promising α-glucosidase inhibitors: an overview. *Eur. J. Med. Chem*. **2019,** 176, 343-377.
22. Kameda, Y.; Asano, N.; Yoshikawa, M.; Takeuchi, M.; Yamaguchi, T.; Matsui, K.; Horii, S.; Fukase, H. Valiolamine, a new α-glucosidase inhibiting aminocyclitol produced by *Streptomyces hygroscopicus*. *J. Antibiot. (Tokyo)* **1984,** 37, 1301-1307.
23. Horii, S.; Fukase, H.; Matsuo, T.; Kameda, Y.; Asano, N.; Matsui, K. Synthesis and α-D-glucosidase inhibitory activity of N-substituted valiolamine derivatives as potential oral antidiabetic agents. *J. Med. Chem*. **1986,** 29, 1038-1046.
24. Crumpstey, I.; Ramstadius, C.; Borbas, K. E.; Alonzi, D. S.; Butters, T. D. Synthesis and α-glucosidase II inhibitory activity of valienamine pseudodisaccharides relevant to *N*-glycan biosynthesis. *Bioorg. Med. Chem. Lett.* **2011**, 21, 5219-5223.
25. Caputo, A. T.; Alonzi, D. S.; Marti, L.; Reca, I. B.; Kiappes, J. L.; Struwe, W. B.; Cross, A.; Basu, S.; Lowe, E. D.; Darlot, B.; Santino, A.; Roversi, P.; Zitzmann, N. Structures of mammalian ER α-glucosidase II capture the binding modes of broad-spectrum iminosugar antivirals. *Proc. Natl. Acad. Sci. USA* **2016,** 113, E4630-E4638.
26. Rawlings, A. J.; Lomas, H.; Pilling, A. W.; Lee, M. J.; Alonzi, D. S.; Rountree, J. S.; Jenkinson, S. F.; Fleet, G. W.; Dwek, R. A.; Jones, J. H.; Butters, T. D. Synthesis and biological characterisation of novel N-alkyl-deoxynojirimycin α-glucosidase inhibitors. *Chembiochem.* **2009**, 10, 1101-1105.
27. Steiner, T.; Koellner, G. Hydrogen bonds with π-acceptors in proteins: frequencies and role in stabilizing local 3D structures. *J. Mol. Biol.* **2001,** 305, 535-557.
28. Warfield, K. L.; Plummer, E. M.; Sayce, A. C.; Alonzi, D. S.; Tang, W.; Tyrrell, B. E.; Hill, M. L; Caputo, A. T.; Killingbeck, S. S.; Beatty, P. R.; Harris, E.; Iwaki, R.; Kinami, K.; Ide, D.; Kiappes, J. L.; Kato, A.; Buck, M. D.; King, K.; Eddy, W.; Khaliq, M.; Sampath, A.; Treston, A. M.; Dwek, R. A.; Enterlein, S. G.; Miller, J. L.; Zitzmann, N.; Ramstedt, U.; Shresta, S. Inhibition of endoplasmic reticulum glucosidases is required for in vitro and in vivo dengue antiviral activity by the iminosugar UV-4. *Antiviral Res.* **2016,** 129, 93-98.
29. de Freitas, R. F.; Schapira, M. A systematic analysis of atomic protein–ligand interactions in the PBD. *Med. Chem. Commun.* **2017,** 8, 1970-1981.

30. Sim, L.; Quezada-Calvillo, R.; Sterchi, E. E.; Nichols, B. L.; Rose, D. R. Human intestinal maltase-glucoamylase: crystal structure of the N-terminal catalytic subunit and basis of inhibition and substrate specificity. *J. Mol. Biol.* **2008,** 375, 782-792.
31. Warfield, K. L.; Alonzi, D. S.; Hill, J. C.; Caputo, A. T.; Roversi, P.; Kiappes, J. L.; Sheets, N.; Duchars, M.; Dwek, R. A.; Biggins, J.; Barnard, D.; Shresta, S.; Treston, A. M.; Zitzmann, N. Targeting endoplasmic reticulum α-glucosidase I with a single-dose iminosugar treatment protects against lethal influenza and dengue virus infections. *J. Med. Chem.* **2020,** 63, 4205-4214.
32. Morris, G. M.; Huey, R.; Lindstrom, W.; Sanner, M. F.; Belew, R. K.; Goodsell, D. S.; Olson, A. J. AutoDock4 and AutoDockTools4: automated docking with selective receptor flexibility. *J. Comput. Chem.* **2009,** 16, 2785-2791.
33. The COVID Moonshot Consortium, COVID moonshot: open science discovery of SARS-CoV-2 main protease inhibitors by combining crowdsourcing, high-throughput experiments, computational simulations, and machine learning. Biorxiv [Preprint] **2020**. https://www.biorxiv.org/content/10.1101/2020.10.29.339317v1.
34. Zhao, X.; Guo, F.; Comunale, M. A.; Mehta, A.; Sehgal, M.; Jain, P.; Cuconati, A.; Lin, H.; Block, T. M.; Chang, J.; Guo, J. T. Inhibition of endoplasmic reticulum-resident glucosidases impairs severe acute respiratory syndrome coronavirus and human coronavirus NL63 spike protein-mediated entry by altering the glycan processing of angiotensin I-converting enzyme 2. *Antimicrob. Agents Chemother.* **2015,** 59, 206-216.
35. Scaman, C. H.; Hindsgaul, O.; Palcic, M. M.; Srivastava, O. P. Synthesis of α-D-Glcp-(1-->2)-α-D-Glcp-(1-->3)-α-D-Glcp-O-(CH2)8 COOCH3 for use in the assay of α-glucosidase I activity. *Carbohydr. Res.* **1996,** 296, 203-213.
36. Berrow, N. S.; Alderton, D.; Sainsbury, S.; Nettleship, J.; Assenberg, R.; Rahman, N.; Stuart, D. I.; Owens, R. J. A versatile ligation-independent cloning method suitable for high-throughput expression screening applications. *Nucleic Acids Res.* **2007,** 35, e45.
37. Otwinowski, Z.; Minor, W. Processing of X-ray diffraction data collected in oscillation mode. *Methods Enzymol.* **1997,** 276, 307-326.
38. McCoy, A. J.; Grosse-Kunstleve, R. W.; Adams, P. D.; Winn, M. D.; Storoni L. C.; Read, R. J. Phaser crystallographic software. *J. Appl. Crystallogr.* **2007,** 40, 658-674.
39. Emsley, P.; Lohkamp, B.; Scott, W. G.; Cowtan, K. Features and development of Coot. *Acta Crystallogr. D Biol. Crystallogr.* **2010,** 66, 486-501.
40. Afonine, P. V.; Grosse-Kunstleve, R. W.; Echols, N.; Headd, J. J.; Moriarty, N. W.; Mustyakimov, M.; Terwilliger, T. C.; Urzhumtsev, A.; Zwart, P. H.; Adams, P. D. Towards automated crystallographic structure refinement with phenix.refine. *Acta Crystallogr. D Biol. Crystallogr.* **2012,** 68, 352-367.
41. Adams, P. D.; Afonine, P. V.; Bunkóczi, G.; Chen, V. B.; Davis, I. W.; Echols, N.; Headd, J. J.; Hung, L. W.; Kapral, G. J.; Grosse-Kunstleve, R. W.; McCoy, A. J.; Moriarty, N. W.; Oeffner, R.; Read, R. J.; Richardson, D. C.; Richardson, J. S.; Terwilliger, T. C.; Zwart, P. H. PHENIX: a comprehensive Python-based system for macromolecular structure solution. *Acta Crystallogr. D Biol. Crystallogr.* **2010,** 66, 213-221.
42. Liebschner, D.; Afonine, P. V.; Baker, M. L.; Bunkóczi, G.; Chen, V. B.; Croll, T. I.; Hintze, B.; Hung, L. W.; Jain, S.; McCoy, A. J.; Moriarty, N. W.; Oeffner, R. D.; Poon, B. K.; Prisant, M. G.; Read, R. J.; Richardson, J. S.; Richardson, D. C.; Sammito, M. D.;

Sobolev, O. V.; Stockwell, D. H.; Terwilliger, T. C.; Urzhumtsev, A. G.; Videau, L. L.; Williams, C. J.; Adams, P. D. Macromolecular structure determination using X-rays, neutrons and electrons: recent developments in Phenix. *Acta Crystallogr. D Struct. Biol.* **2019,** 75, 861-877.

43. Sanner, M. F. Python: a programming language for software integration and development. *J. Mol. Graph. Model.* **1999,** 17, 57-61.

For Table of Contents Only

Table of Contents Graphic

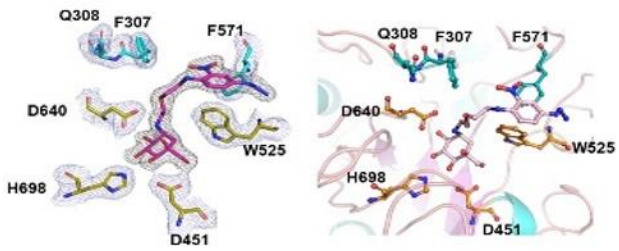

α-GluII-valiolamine derivative complex
Crystal Structure